WIRE ELECTRICAL DISCHARGE MACHINING OF HELICAL DEVICES FROM PERMANENT MAGNETS

by

Jeremy Greer

A thesis submitted to the faculty of
The University of Utah
in partial fulfillment of the requirements for the degree of

Master of Science

Department of Mechanical Engineering

The University of Utah

December 2011

The University of Utah Graduate School

STATEMENT OF THESIS APPROVAL

The thesis of **Jeremy Greer**

has been approved by the following supervisory committee members:

Eberhard Bamberg	, Chair	**8/25/11** Date Approved
Jake J. Abbott	, Member	**8/25/11** Date Approved
K. L. DeVries	, Member	**8/25/11** Date Approved

and by **Timothy Ameel** , Chair of

the Department of **Mechanical Engineering**

and by Charles A. Wight, Dean of The Graduate School.

ABSTRACT

Microrobots are desired for future minimally invasive medical applications. One promising area of this field is the use of screws and helical swimmers, which can be propelled and controlled by the use of external magnetic fields to induce torque or force in the microrobot. These devices have possible applications in areas such as the eye, prostate, and kidneys to name a few. This research focuses on the fabrication of screws made of neodymium-iron-boron rare earth magnets.

Rare earth magnets are brittle and are not easily machined through conventional methods. A wire electrical discharge machine was used to fabricate the devices described in this thesis. Initial test cutting showed slow machining times; therefore a Taguchi design of experiments was used to find the optimal settings for the wire electrical discharge machine. Further analysis was done to analyze the loss in permanent magnetic field in the magnets due to heating in the machining process. Finally, a fabrication method for machining the helical geometry in the magnet was developed for use on the three-axis wire electrical discharge machine. Three prototypes were manufactured and data showed that the permanent magnetic field remained intact and that torques could be induced in the machined magnets.

CONTENTS

LIST OF FIGURES

LIST OF TABLES

ACKNOWLEDGEMENTS

I would like to thank my committee members: Eberhard Bamberg for his assistance and expertise with the EDM, Jake Abbott for input on the design of the helical devices and for funding this project, and Larry DeVries, whose door was always open to my questions. I would like to thank my fellow students, namely Arthur Mahoney and Andrew Petruska, for their contributions to this work. Finally I would like to thank my family and ever faithful wife, Meghan.

1 INTRODUCTION

1.1 Project Definition

The purpose of this project was to create magnetic devices such as screws and helical swimmers. This was done by cutting threads, using a wire electrical discharge machine (WEDM), into a diametrically magnetized rare earth magnet. The magnet used was a neodymium-iron-boron (NdFeB) type magnet with a nickel-copper-nickel coating to inhibit corrosion. Not much is found in the literature about the cutting parameters of NdFeB on the WEDM. Different types of helical devices have been fabricated utilizing different methods, but none have been fabricated out of a permanent magnet. Helical devices have potential applications in medicine to perform tasks that would normally require invasive surgeries or therapy. Because of their small relative size, fabrication of helical devices, particularly out of NdFeB, is nontrivial. This research served to develop a fabrication method for a helical device using a three-axis WEDM.

1.2 Objectives

The main objectives of this research were to:

1. Characterize and optimize the cutting parameters of NdFeB magnets.
2. Determine the nature and extent of the loss of permanent magnetic field due to heating from the WEDM process.
3. Develop a fabrication method for helical devices on a three-axis WEDM.

Initial test cutting and published research has shown that WEDM cutting of NdFeB is relatively slow [1]. Therefore, a main goal of this research was to find the optimal cutting parameters on the WEDM to manufacture the helical devices. A Taguchi analysis was used, similar to other experiments done for any type of machining process [2]. This would enable minimal manufacturing time, and a more accurate part, due to the characterization of the kerf loss.

A main area of interest in this research is to determine the magnetic loss due to heat from machining of the magnet on the WEDM. When the magnet is heated above its Curie temperature, it looses its magnetization [3]. Since a portion of the magnet being machined in the WEDM is necessarily heated above the Curie temperature to be melted off, a portion of the magnet must also suffer a loss of the permanent magnetic field. Nothing is found in the literature about this loss of permanent magnetic field due to WEDM. Most magnets are manufactured net shape, and when WEDM machining is used to further shape the magnet, it is usually magnetized postmachining [4]. A finite element analysis and experimental torque measurements were used to determine the extent of the demagnetized layer in the permanent magnet.

The third main objective of this research was to develop a fabrication method for helical devices in the WEDM. The WEDM used for this research is a three-axis machine: two translational axes and one rotational axis. Similar geometries to screws and helical swimmers, such as end mills, have been made using WEDM, but utilize a six-axis machine [5]. The WEDM is an advantageous choice over conventional machining methods because it is a thermal process and not a mechanical process, yielding less chipping and cracking due to mechanical failure; this will be useful for sintered NdFeB magnets, which exhibit high hardness, low ductility, and a tensile strength of approximately 100 MPa [1]. The WEDM can also yield a high degree of dimensional accuracy, using wire sizes down to 20 μm, with the width of cut, known as kerf, slightly larger depending on machine parameters.

1.3 Motivation

Medical procedures are moving toward minimally invasive methods. Where once open heart surgery was required, now a standard procedure is catheterization through the femoral artery. Where once the removal of the appendix required opening the abdomen of a patient, now the appendix can be removed laparoscopically. This movement toward minimally invasive procedures yields several advantages for the patient. Recovery time and postoperative pain is reduced, as well as a reduction in the risk of infection. This trend toward minimally invasive methods demands more innovative methods to perform procedures in vivo. Microrobots are a promising area of research that could be used to perform surgical tasks [6].

Microrobots could be used to deliver drugs and radioactive seeds, as well as used for increasing the temperature of a local area for hyperthermia or thermoablation [6]. This heating would most likely take place through the use of high-frequency magnetic fields or ultrasonic resonating mechanical structures. Microrobots could also be utilized for material removal, such as the removal of deposits in blood vessels or the removal of stones from an organ. Structures such as a stent, electrodes, or scaffold could also be placed remotely by using microrobots. Telemetry and sensing such as chemical concentrations or location of bleeding could also be obtained by microrobots.

Some areas of the body where microrobots show promise for application include the circulatory system, the urinary system, the prostate, and the eye [6]. Applications for the circulatory system include drug delivery, breaking up blood clots, removing plaque, and acting as or placing of stents. A major difficulty of applying microrobots in the circulatory system is overcoming the force of the blood flow. Research has shown that this is possible albeit challenging [6]. A microrobot could be used to break up kidney stones by swimming up the ureter. Microrobots also have potential for the treatment of prostate cancer. Prostate cancer is commonly treated by placing a radioactive pellet in the prostate to kill tumors; this is known as brachytherapy. The pellet is placed by a needle inserted through the perineum, which contains densely populated nerves, or through the colon, which caries a high risk of infections. The prostate also deforms and displaces due to the force of the needle, inhibiting precise placement. Microrobots, particularly the screws proposed for this research, could have application for reducing the invasiveness of placing the radioactive pellet and could overcome problems of the prostate moving by drilling through the tissue instead of piercing and pushing through the tissue. Applications for the eye have been proposed by wirelessly controlling a microrobot with magnetic fields and tracking through the pupil visually [7]. The OctoMag system described by Kummer *et al.* [7] could be used to propel the types of screws developed herein to deliver drugs to the retina without first requiring the removal of the vitreous.

2 NEODYMIUM IRON BORON MAGNETS

2.1 History

Prior to mainstream use of rare earth magnets such as NdFeB magnets, Alnicos and ferrites were most commonly used in magnetic devices. Rare earth magnets have higher energy products, (BH_{max}), a measure of the quality of a magnet, and enable smaller magnets to be used in devices [4]. The first rare earth magnets, samarium-cobalt magnets, are credited to Velge and Buschow at Phillips in 1967 by bonding $SmCo_5$ powder in a resin [4]. These magnets were first implemented in small applications such as stepper motors and headphones. In the 1970s shortages in the world's cobalt supply led to a search for additional types of rare earth magnets [4]. In 1983 Sagawa announced that Sumitomo had created a $Nd_{15}Fe_{77}B_8$ magnet [4]. Further varieties of NdFeB magnets have been developed and are used in applications in motors, robotics, and medical imaging.

2.2 Process

The NdFeB magnets used in this research were made using a sintering process [4]. The raw material is produced by a chemical reaction in a vacuum induction furnace. The material is then jet milled into a fine powder (≈3μm). The powder is "die upset" pressed so that it has a preferred magnetization direction. The powder is hot pressed at ≈725°C into a die. The material is then pressed again, decreasing the height and increasing the length of the workpiece. This creates the preferred direction of magnetization parallel to the direction of the pressing motion. The workpiece is then sintered at an elevated temperature, below the melting point, until the particles adhere to each other. The bare magnets are prone to oxidation and lose their magnetization in the presence of moisture; therefore protective plating is applied. In this case it is a Ni-Cu-Ni coating 15-21μm thick [8]. The magnets are finally magnetized by placing them in a very strong magnetic field.

2.3 Magnet Properties

A typical magnetization curve is shown in Figure 2.1. A unmagnetized magnet is magnetized by placing it in a strong magnetic field, typically generated by a high current electromagnet. The generated field (H) is increased to a “saturation point” at which an increase in generated field will not increase the residual flux density of the magnet (B). If the applied field does not reach the saturation point, the generated hysteresis loop will be a minor loop contained within the major loop. When the generated field is removed, the residual flux density, B_r, is the remaining residual flux density of the magnet, which gives the permanent magnet its magnetic strength.

The coercivity (H_C) of magnet is a measure of the strength of the applied field necessary to drive the magnetization of the permanent magnet to zero after it has been driven to its saturation point. Coercivity, sometimes called coercive force or coercive field, is usually measured in Oersteds or Amperes/meter. A final parameter, maximum energy product (BH_{max}), is obtained at the point where B·H is maximized. BH_{max} is where the potential energy of the magnet is maximized and is quantified in J/m^3. NdFeB magnets have been produced with a BH_{max} of up to 400 kJ/m^3[3,9].

Table 2.1 shows some typical properties of different types of magnets. NdFeB magnets are ideal for the application of small helical medical devices because of the large BH_{max} quantity, which enables a large amount of torque to be generated with a given applied field when compared to other types of magnets.

2.4 Material Properties

Despite the "rare earth" name, abundances of these substances in the earths crust rank with zinc or lead [4]. Neodymium is the most abundant magnetic rare-earth element. The first compound, produced by Sumitomo, was $Nd_{15}Fe_{77}B_8$, but several other formulas and additions of elements have been made. Dysprosium, niobium, and aluminum have been added to increase coercivity. Vanadium and cobalt have been added to increase coercivity, Curie point, and corrosion resistance. NdFeB magnets are brittle and hard, measuring 560-600 on the Vickers scale, just below tool steel [10]. Consequently, traditional machining methods are not recommended. EDM and wire saw are usually used when further manufacturing is needed beyond the sintering process. Traditional machining methods also generate heat, which can demagnetize the magnet, and the powder produced when cutting is flammable.

NdFeB magnets have a melting temperature of over 1000°C, although the material does not melt congruently[11]. The actual working temperature of the magnet is much lower. When a magnet is heated above what is known as the Curie temperature, the orientation of the electron spin in the atoms becomes randomized and the permanent magnetic field is removed [3]. At lower elevated temperatures, a portion of the magnetic field is diminished due to the same reasoning. The temperature at which the field begins to be affected is the maximum operating temperature. The magnets used for this work have a maximum operating temperature of 80°C and a Curie temperature of 310°C [8].

2.5 Uses

Rare earth magnets, including NdFeB magnets, have found applications in everything from motors and actuators to magnetic resonance imaging (MRI) machines [12]. Ceramic ferrite type magnets have long been used in DC electric motors, but rare earth magnets have been used for the advancement of brushless DC motors [3]. Because of the high energy of rare earth magnets, greater torques can be achieved because of greater air gap flux densities over traditional magnets [3]. Greater coercivity when compared to traditional magnets is also advantageous because it decreases demagnetization due to the motors armature winding. Rare earths have also been used in computer hard disks, both for the spindle motor and the coil actuator of the read/write head [4]. This is advantageous because minimizing the time required to access different areas of the disk platters requires high forces, more easily achievable with rare earths over traditional magnets. Magnetic position sensors have also benefited from the increased energy densities of rare earth magnets [3]. These types of magnets allow for greater air gaps (allowing for greater tolerances) to be used, or to increase the sensitivity of the sensor system.

MRI machines, used for medical diagnosis and animal inspection in the food industry have also benefited from the development of rare earth magnets [4]. MRI requires very uniform fields, which were originally created using superconducting coil electromagnets. Early MRI scanners used fields up to 1.5 T, but advances in scanners have allowed for lower field to be used, in the 0.1-0.5 T range [3]. Furthermore, smaller machines have been developed for specific applications, such as scanning a limb or head, reducing the cavity space required to contain the uniform field. This allows for permanent magnets to be used to create the field. Different shaped arrays of magnets have been designed to create the field in the array, including a square, triangular, and round tube. Methods have also been developed to mitigate the end effects of such magnet tube arrays. Figure 2.2 shows an example triangular array used to create a uniform field in a cavity that could be used in a MRI type application. The small arrows indicate the orientation of the constituent magnets, and the large arrow is the orientation of the field in the cavity.

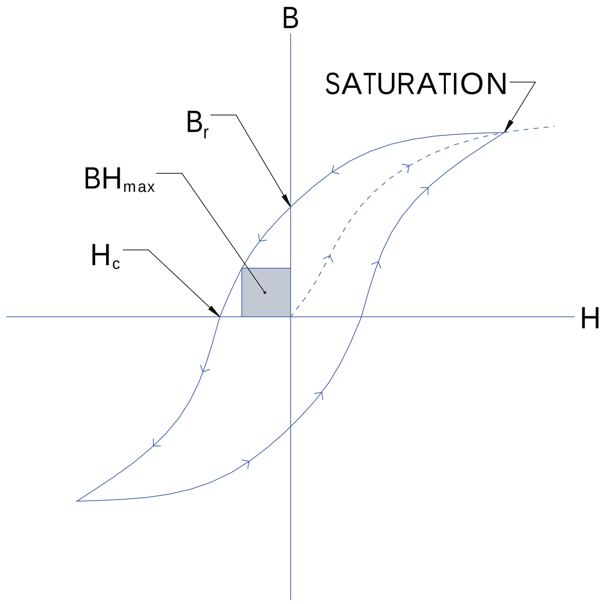

Figure 2.1- Hysteresis loop for permanent magnet, adapted from Coey [4]

Table 2.1-Typical properties of some magnets [4]

Type	Main Phase	B_r (T)	H_c (kA/m)	BH_{max} (kJ/m^3)
Ferrite	$SrFe_{12}O_{19}$	0.39	265	28
Alnico V	$Fe_{48}Al_{16}Ni_{13}Co_{21}Cu_2$	1.28	52	43
Sm-Co	$SmCo_5$	0.88	680	150
Sm-Co	$SmCo_{17}$	1.08	800	220
Nd-Fe-B	$Nd_2Fe_{14}B$	1.25	920	300

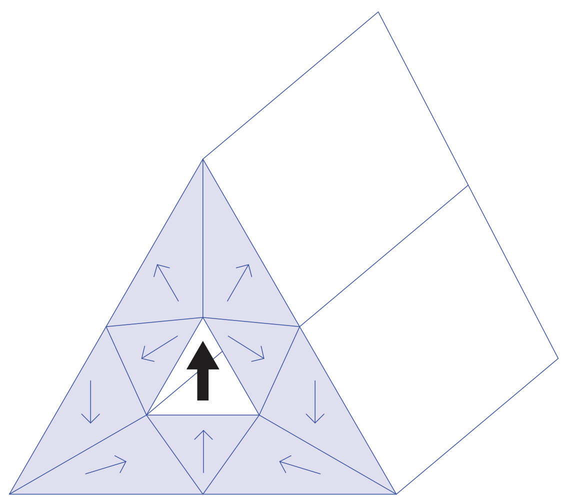

Figure 2.2- Triangular array creating uniform field in cavity, adapted from Coey [4]

3 ELECTRICAL DISCHARGE MACHINGING

3.1 History

The EDM process was developed during the same time period by the USSR and the USA near the beginning of the World War II [13]. During the war, critical materials, such as tungsten, needed to be conserved. Tungsten was used as electrical contacts in ignition systems and was subject to pitting and erosion over time. The USSR government assigned Dr. Boris Lazarenko and Dr. Natalya Lazarenko to determine if the life of the components could be extended. Their work included an experiment where the electrical contacts were submerged in oil. The oil did not eliminate the unwanted sparking, but it did enable more uniform and predictable sparking. Ultimately, this was not a successful method to reduce pitting and reduce the usage of tungsten, but it led to more investigation of the sparking process. The Lazarenkos eventually developed a servo controlled machine to maintain the spark gap and many of their machines were used during the war era to machine difficult to machine materials like tungsten and tungsten carbide. Their machines used a resistor capacitor (R-C) circuit sometimes referred to as a Lazarenko type machine [13].

During the same time period, but separate from the Lazarenko's work, a company in the USA needed a method to remove broken taps and drills [13]. The tools were being broken off in expensive aircraft parts. Harold Stark, Victor Harding, and Jack Beaver were assigned to remove the broken tools and salvage the parts. Their process started by using an electric etching tool to produce the sparks. Eventually they built a more powerful version of the etching tool to increase speed. The tool produced large amounts of molten material that needed to be removed from the work area. Initially, compressed air was used with limited success. Then it was determined that water could be used as a coolant and to flush the area. They eventually created an automated process that involved the use of an electromagnet to lift the electrode off the workpiece when the spark was initiated. Then gravity pulled the electrode back toward the workpiece when the spark ceased and the electromagnet was turned off. Similar to the Lazarenko's machines, many of these machines were utilized in the USA during the war. After leaving the company, Stark, Harding, and Beaver were allowed to patent their system. Their developments served as the basis for the vacuum tube EDM machine and a servo system that maintained proper spacing between the electrode and the workpiece. This increased the sparking frequency from 60 times per second to 1,000's of times per second.

Later in the 1960s and 1970s the wire EDM was developed. It used a continuously fed wire to replenish the worn electrode and was increasingly useful with the advent of numerically controlled (NC) machines. The USSR presented a WEDM machine at a machine exposition in 1967 that is credited with being the first commercially available WEDM [13]. Today modern computer numerically controlled (CNC) systems and transistor type power supplies and switching systems are used on many commercial machines. They allow for greater control of machining parameters, such as spark on and off time, current, and voltage of the machine. The R-C type machines are still used where fine surface finish is required and for drilling of small holes.

3.2 Process

At the most basic level, the EDM material removal process occurs when an electrode at a high voltage potential is brought close to the work piece in a dielectric medium. When the distance between the work piece and the electrode is sufficiently small enough that a spark occurs, material is removed from the electrode and the work piece. The dielectric fluid is flushed through the spark area to remove material and thermally control the machined surface. Typically, though not always, the dielectric fluid is oil for conventional EDM and de-ionized water for WEDM. The work piece is typically submerged in a tank of the dielectric fluid to maintain thermal stability and aid in the flushing of removed material. The material removal process is deemed nontraditional because it occurs due to thermal processes, not mechanical processes as in conventional machining. In a conventional EDM, as the electrode is eroded away it maintains the spark gap by continually feeding the electrode toward the machined surface. In a wire EDM the electrode is continually replaced by a wire spool system so that the diameter of the electrode remains constant. The spark gap is maintained by bringing the wire toward the direction of cutting with respect to the work piece.

At a smaller level, when the spark occurs, it creates a plasma channel. Temperatures within the region are between 8,000°C and 12,000°C [14] and may be as high as 20,000°C [15]. The material is vaporized by the spark. When the spark is turned off, the plasma channel breaks down and the molten particle resolidifies and is flushed away in the dielectric fluid. The high temperatures created during the machining process can affect the properties of the workpiece material. When the spark ceases, some of the vaporized material can be re-deposited onto the workpiece. This re-deposited layer can contain elements of the electrode and the dielectric fluid. The region below the re-deposited layer can become hot enough to melt, but not vaporize. This will affect the material properties of the region and is known as the resolidified layer. The combination of the redeposited layer and the resolidified layer is known as the recast layer. The region below the resolidified layer can also become hot enough to alter the material properties of the parent material. The heat affected zone (HAZ) is the whole area that the material properties have been altered due to spark heating. The heat affected zone is of particular interest when machining NdFeB magnets because when the magnet is heated above the Curie temperature the material becomes unmagnetized, essentially losing its permanent magnetic field. Although the HAZ negatively affects the performance of magnets machined in this research, the loss of magnetic strength is shown to be small in comparison to the size of the workpiece. Figure 3.1 shows the heat affected zone due to WEDM.

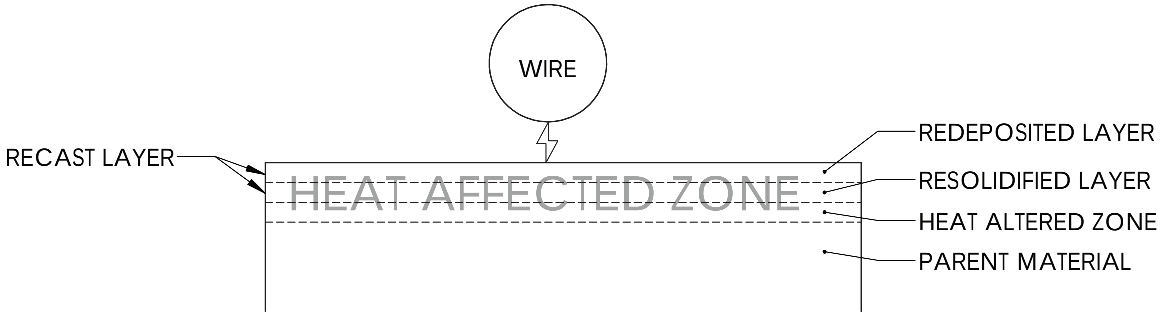

Figure 3.1- Diagram of heat affected zone (HAZ)

4 MACHINING HELICAL DEVICES

4.1 Current Devices

Very small (≈ 3 μm diameter) helical swimming devices have been manufactured by a process of crystal growth and photolithography [16]. These were propelled by a soft magnetic head that was attached and used for applying torque to the swimmer. SiO_2 chiral structures 200-300 nm diameter have also been fabricated by a shadow growth method [17]. Further research has been done involving a helical swimmer of 1 mm diameter made from Nitinol tubing [18]. This was made using a WEDM to cut the helix out of a piece of tubing. A magnet was then bonded to the swimmer after machining for propulsion. Other devices have been fabricated by wrapping a tungsten wire around a ceramic "pipe", 1.2 mm diameter and 15 mm long [19]. Still other devices have been made by bonding a brass wood screw tip to a diametrically magnetized cylindrical magnet [20]. The helical screws made for this research most closely resemble this last type of device, with a thread similar to a wood screw cut into the body of a diametrically magnetized cylindrical magnet.

4.2 Machine Setup

4.2.1 WEDM Machine

The wire electrical discharge machine used for this research is a R-C type machine as described earlier and was constructed under the direction of Dr. Eberhard Bamberg at the University of Utah. It was designed to be primarily used for manufacturing of components for miniature mechanical systems and microelectro-mechanical systems (MEMS) [21]. The machine has also been used in research of cutting of semiconductor materials such as germanium and silicon [22,23]. It has a footprint of less than one square meter and a wide set of operating parameters to adapt to different materials and machining conditions. The WEDM used is a three-axis machine; it consists of two translational axes and a rotary axis. The wire lies on the X axis, and can be translated along the Y and Z axes relative to the part. The part can also be rotated about the B axis, which can be oriented to lie at any angle, θ, in the horizontal (i.e., X-Y) plane, as shown in Figure 4.1.

The wire guides can be adjusted to span between 0-250mm to allow a wide array of geometries to be accommodated. The wire is mounted horizontally as opposed to vertically like most commercially available WEDM. This allowed for a design of a smaller, shallower, dielectric tank to be used with a wide range of distances for the wire guides. The WEDM is shown in Figure 4.2. The wire system consists of a wire puller, a brake, and a tension sensor. The wire puller pulls the wire at a given input speed and collects the used wire for later disposal. The wire brake, a Magtrol HB-450 hysteresis brake, enables smooth rotation at slow RPM. The brake resists the motion of the wire puller and keeps the wire taut at the specified tension. The brake grips the wire by applying a torque to a rubber wheel, while a second wheel is tensioned against the rubber wheel; this eliminates wire slippage in the system. The tension is measured by a Honigmann RFS 150 tension sensor; this provides feedback to the control system and enables the brake to constantly adjust in order to maintain wire tension. Tensions as low as 1 N are allowable in order to accommodate small (20 μm) diameter wires. The wire can be fed through the machine at speeds between 0 and 250 mm/s with wire tensions ranging from 1-200 N.

The control system and spark generation system were created by Optimation, LLC and adapted by Dr. Eberhard Bamberg toward research in cutting semiconductor materials. The wire tension system, as well as the motion control of the three axes, is controlled by the proprietary software and electronics. A notable feature of the control system is the ability to optimize the feed rate of the machine by examining the ratio between the frequency of shorts and the frequency of sparks of the wire. In order for sparking and subsequent machining to take place, the spark gap between the wire and the workpiece must be maintained. If the wire contacts the workpiece, the circuit is shorted and no material is removed. Most commercial machines set feed rates sufficiently slow that the wire never shorts on the work piece. This approach works, but may be slow. The machining rates are usually determined from experience and knowledge of the material being machined and the manufactures tabulated values. In the case of this machine, exotic materials are being used and therefore not much is initially known about the cutting characteristics of a given material. The control software of this WEDM adjusts the speed by detecting when shorts occur. When the machine shorts, it must back up to re-approach the spark gap. This reduces the overall feed rate and increases machining time. By slowing the feed to an optimal ratio of shorts and sparks, it allows the machine to feed at the fastest possible rate for the given input parameters. The spark parameters can also be adjusted between 0 and 300V and a wide range of capacitors can also be used, commonly 3.3nF to 33nF.

4.2.2 Rotary Table

Normally helical geometries cut on a WEDM require 4+ axis machines to achieve accurate geometry. Since a 4+ axis machine was not available for this research, the following method was used to cut the helical geometries.

A screw thread is defined in mathematical terms as a helix. When the helix is viewed perpendicular to its axis of rotation, the projected view is a sine wave. A sine wave is defined as

$$y(x) = A\sin(\omega x + \varphi) \tag{1}$$

where A is the amplitude of the sine wave, ω is the angular frequency, x is the independent variable, and φ is the phase (where in its cycle the oscillation begins at x = 0). The amplitude of the sine wave corresponds to the radius of the helix in the screw thread. The slope of the line tangent to a sine wave at the x-axis can be found by setting φ = 0 and differentiating at x = 0 which yields

$$\frac{dy}{dx} = A\omega\cos(\omega x) \tag{2}$$

In order to accurately machine threads on the screws, the wire was set tangent to the sine wave of the helix. Since the radius at the bottom of the thread and the radius at the top of the thread are different, the top and the bottom of the thread will have a different amplitude of sine wave. This will yield two different sine waves, and two different slopes of tangent lines. The angle of the tangent line with respect to the y-axis can be found by taking the inverse tangent of the reciprocal of the slope of the line. The average of the angles between the outer diameter tangent line and the inner diameter tangent line was used as the angle of rotation, θ, for the rotational axis. Figure 4.3 illustrates this. The angle, θ, of the average tangent line was used to rotate the rotary axis (B-axis) of the WEDM as shown in Figure 4.4.

Because the average angle of rotation, θ, is used instead of the exact angle of rotation for a given point in the helix, an error is introduced. This error, called overcut, occurs when excessive material is machined into the sides of the screw threads. Since the material in these areas is not desired to be machined, it is "overcut." This overcut is illustrated as the shaded portions in Figure 4.5. This overcut error was small (<0.010mm), and was deemed acceptable for this experiment. Because the intended application of the helical devices designed herein is in soft tissue, small deviations from an idealized helical geometry will have negligible effects.

The screw threads were machined by making multiple passes on the workpiece. The pattern of cutting that yielded the least amount of wire breakage was to machine the groove of the thread with increasing depth, similar to single point threading on a lathe, as shown in Figure 4.6.

4.2.3 G-Code Generation

The following method was used to generate the g-code used by the WEDM to cut the helical devices. The profile of the modeled helical device was plotted normal to the plane of the Y-Z axis of the WEDM. Circles, the diameter of the kerf, were then plotted, overlapping along the contour of the screw thread. The locations of these circles, which is where the wire will travel and remove material, were then measured as shown in Figure 4.7. The machining points were then given letter designations (A,B,C…) in ascending order of the Y axis values. The points were tabulated in a spreadsheet as shown in Table 4.1. The degrees rotation is the amount of degrees the rotary table will rotate while cutting a given point in the helix. The ending point (Y end) was determined from the point at which the wire would begin to cut past the end of the workpiece. This is illustrated in Figure 4.8. The data points were then sorted into descending order of Z values, as depicted in Figure 4.6, to gradually increase the depth of cut. The sorted data points are shown in Table 4.2.

Finally, these points were input into a Matlab program used to generate the g-code used by the WEDM. The Matlab program can be found in Appendix A. The general pattern of machining is to start at the beginning of the thread, then translate in the –Y direction while rotating the B axis. The wire is then lifted in the Z direction, taken back to the start of the thread, and then repeated with the next machining point.

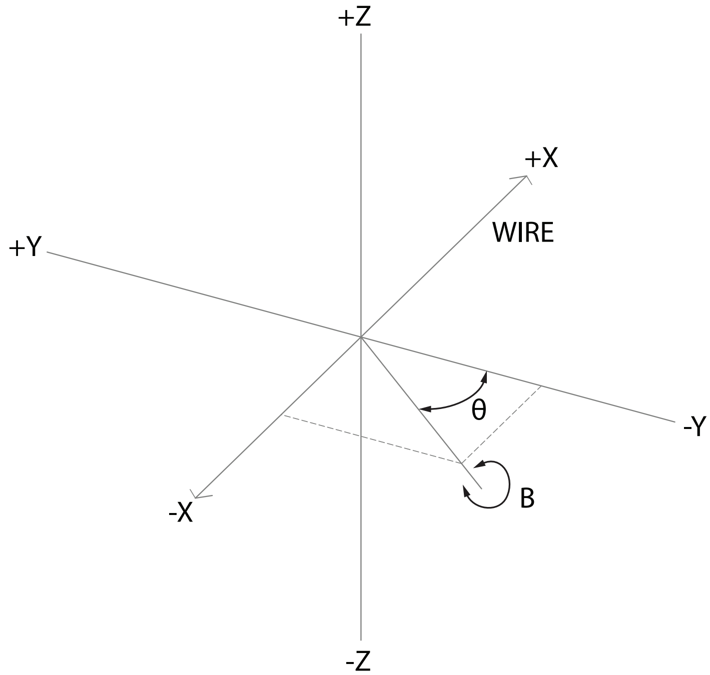

Figure 4.1-Coordinate system of WEDM

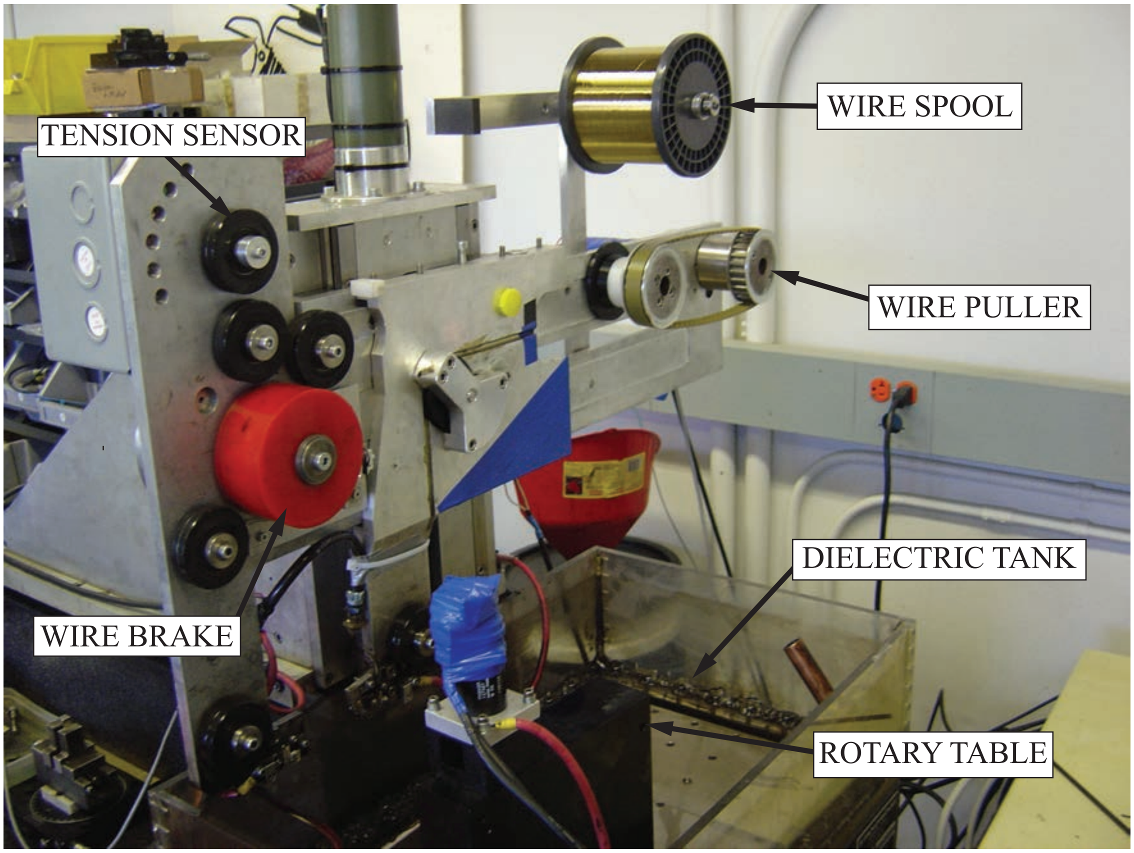

Figure 4.2- WEDM used for this research

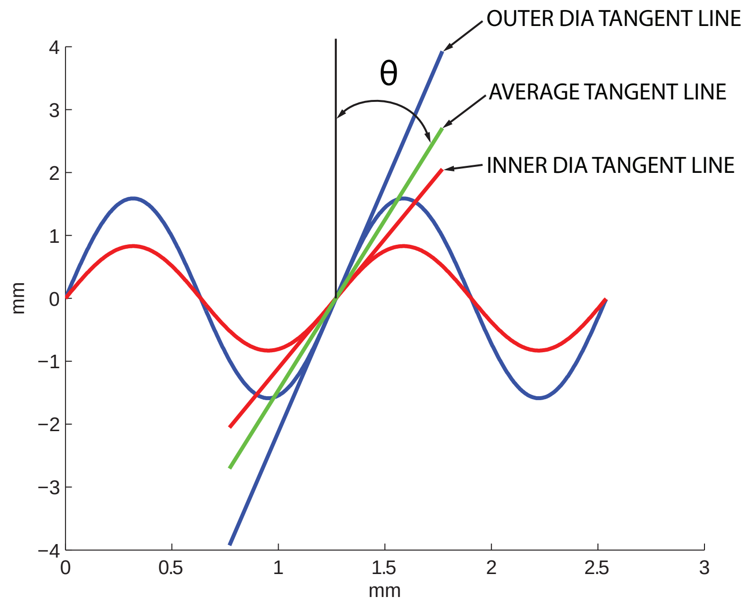

Figure 4.3-Rotary axis alignment

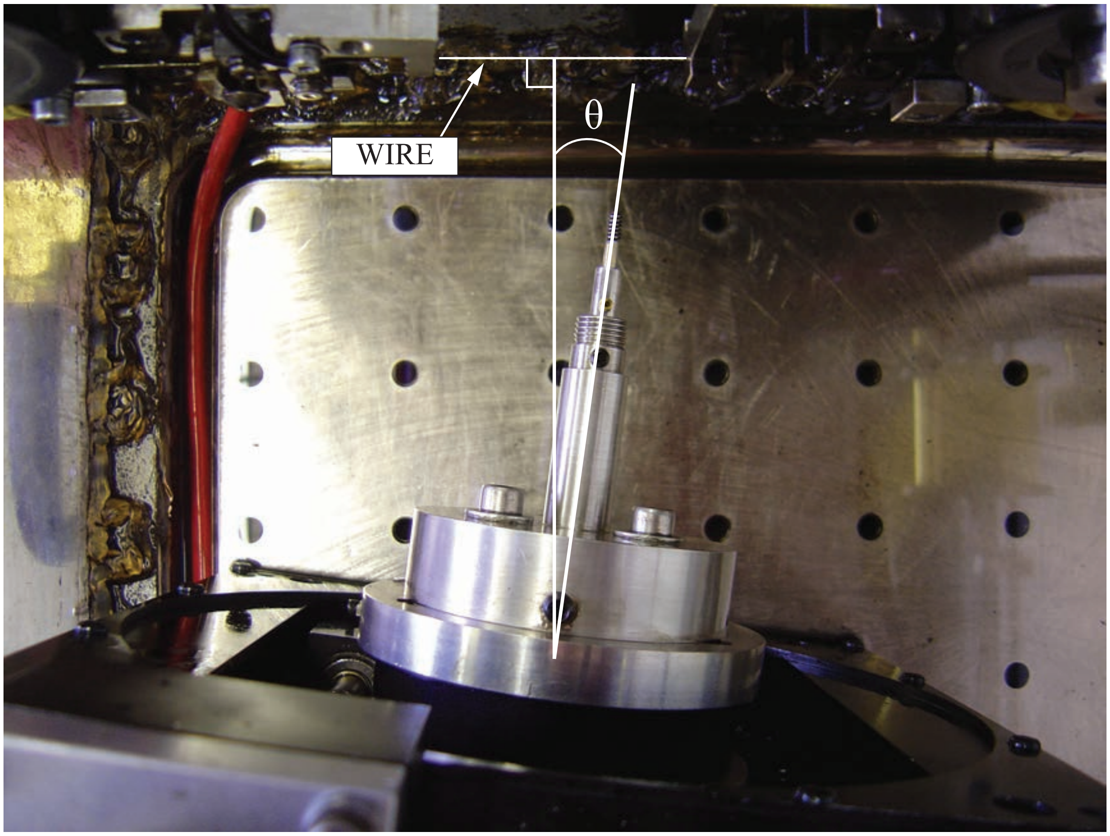

Figure 4.4- Rotary table setup

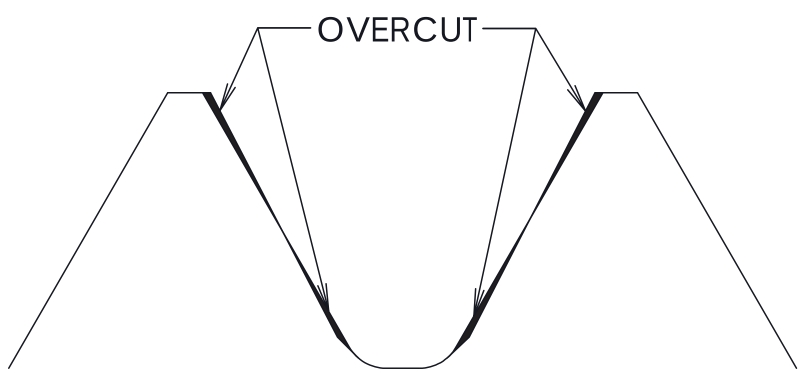

Figure 4.5- Exaggerated illustration of overcut error (shaded areas) in machined threads

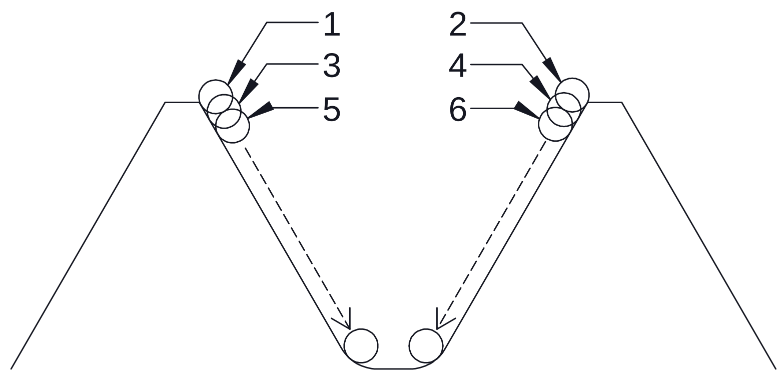

Figure 4.6- Machining pattern for screw thread form

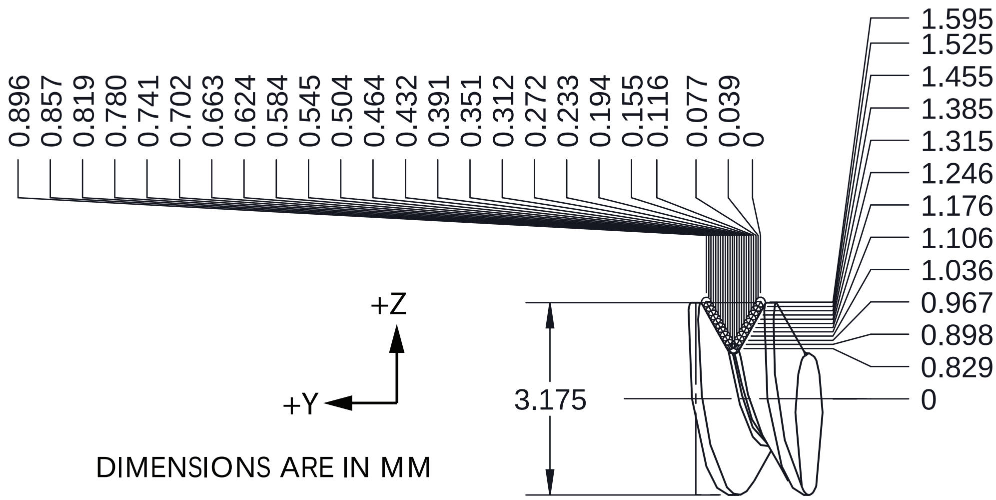

Figure 4.7- Location of machining points for cutting a screw.

Table 4.1- Machining points for g-code generation

	Data Point	Y Start (mm)	Z (mm)	Y End (mm)	Rotation (°)
1	**A**	**0.000**	**1.595**	**-6.244**	**-1800.1**
2	**B**	**0.039**	**1.525**	**-6.244**	**-1811.3**
3	**C**	**0.077**	**1.455**	**-6.244**	**-1822.3**
4	**D**	**0.116**	**1.385**	**-6.244**	**-1833.5**
5	**E**	**0.155**	**1.315**	**-6.244**	**-1844.8**
6	**F**	**0.194**	**1.246**	**-6.244**	**-1856.0**
7	**G**	**0.233**	**1.176**	**-6.244**	**-1867.3**
8	**H**	**0.272**	**1.106**	**-6.244**	**-1878.5**
9	**I**	**0.312**	**1.036**	**-6.244**	**-1890.0**
10	**J**	**0.351**	**0.967**	**-6.244**	**-1901.3**
11	**K**	**0.391**	**0.898**	**-6.244**	**-1912.8**
12	**L**	**0.432**	**0.829**	**-6.244**	**-1924.6**
13	**M**	**0.464**	**0.829**	**-6.244**	**-1933.9**
14	**N**	**0.504**	**0.898**	**-6.244**	**-1945.4**
15	**O**	**0.545**	**0.967**	**-6.244**	**-1957.2**
16	**P**	**0.584**	**1.036**	**-6.244**	**-1968.5**
17	**Q**	**0.624**	**1.106**	**-6.244**	**-1980.0**
18	**R**	**0.663**	**1.176**	**-6.244**	**-1991.2**
19	**S**	**0.702**	**1.246**	**-6.244**	**-2002.5**
20	**T**	**0.741**	**1.315**	**-6.244**	**-2013.7**
21	**U**	**0.780**	**1.385**	**-6.244**	**-2025.0**
22	**V**	**0.819**	**1.455**	**-6.244**	**-2036.2**
23	**W**	**0.857**	**1.525**	**-6.244**	**-2047.2**
24	**X**	**0.896**	**1.595**	**-6.244**	**-2058.4**

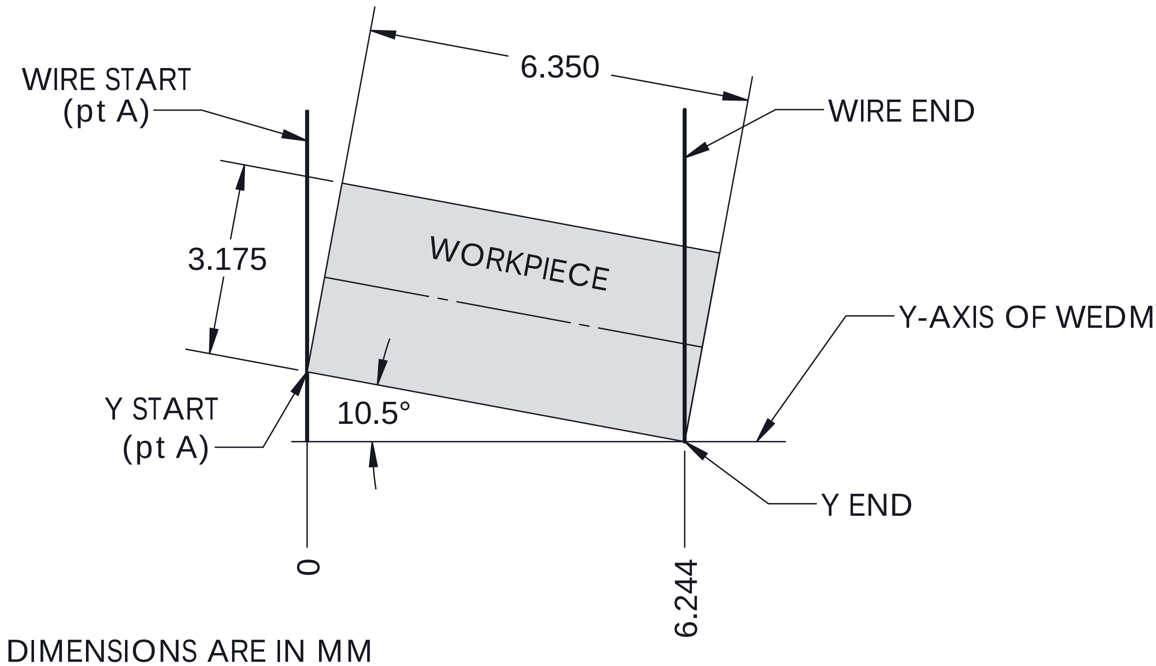

Figure 4.8- Top view of setup of workpiece in WEDM

Table 4.2- Sorted machining points for g-code generation

	Data Point	Y Start (mm)	Z (mm)	Y End (mm)	Rotation (˚)
1	A	0.000	1.595	-6.244	-1800.1
2	X	0.896	1.595	-6.244	-2058.4
3	B	0.039	1.525	-6.244	-1811.3
4	W	0.857	1.525	-6.244	-2047.2
5	C	0.077	1.455	-6.244	-1822.3
6	V	0.819	1.455	-6.244	-2036.2
7	D	0.116	1.385	-6.244	-1833.5
8	U	0.780	1.385	-6.244	-2025.0
9	E	0.155	1.315	-6.244	-1844.8
10	T	0.741	1.315	-6.244	-2013.7
11	F	0.194	1.246	-6.244	-1856.0
12	S	0.702	1.246	-6.244	-2002.5
13	G	0.233	1.176	-6.244	-1867.3
14	R	0.663	1.176	-6.244	-1991.2
15	H	0.272	1.106	-6.244	-1878.5
16	Q	0.624	1.106	-6.244	-1980.0
17	I	0.312	1.036	-6.244	-1890.0
18	P	0.584	1.036	-6.244	-1968.5
19	J	0.351	0.967	-6.244	-1901.3
20	O	0.545	0.967	-6.244	-1957.2
21	K	0.391	0.898	-6.244	-1912.8
22	N	0.504	0.898	-6.244	-1945.4
23	L	0.432	0.829	-6.244	-1924.6
24	M	0.464	0.829	-6.244	-1933.9

5 RESULTS

5.1 Parameter Optimization with Taguchi Design of Experiment

5.1.1 Design of Experiment

Initial test cutting of NdFeB magnets proved to be very slow, with machining rates as low as 0.01mm^2/s and machining times for helical geometries of 100+ hours. It was desired to decrease the machining time and determine the correct kerf offset to accurately machine screws. A design of experiments (DOE), was planned using the Taguchi methodology. Taguchi methods include the use of signal to noise (SN) ratios and orthogonal arrays to design the experiment. Taguchi design of experiments has several advantages over other design of experiment methods. It can greatly reduce the number of experiments required, compared to a full factorial design. In the case of this experiment it reduced the number of experiments from 27 for a full factorial design to 9 for the Taguchi method. Similar DOE's have been performed for the analysis of WEDM parameters for gallium doped p-type germanium [24].

The orthogonal array used for this experiment is the L9 array and is shown in Table 5.1. The numbers in the four rightmost columns of the orthogonal array represent different levels of the control parameters of the experiment. The L9 orthogonal array can experiment on as many as four factors of three levels, although four factors are not necessary for proper Taguchi analysis [2]. The control parameters for this experiment are capacitance, voltage, and polar direction of the permanent magnet samples. The output parameters used for this experiment are the slicing rate, kerf loss, and variation in kerf. The slicing rate is the product of feed rate and workpiece thickness. It is measured in area/time, in this case mm^2/min. In order to determine the volumetric material removal rate, one would multiply the slicing rate by the kerf.

The polar direction of the permanent magnet is the direction from the south to the north pole of the magnet in the coordinate system of the WEDM as illustrated in Figure 4.1. The polar direction is of particular interest because of the force on the current carrying wire, called the Lorentz force, or Ampere's force, governed by

$$\vec{F} = L\left(\vec{i} \times \vec{B}\right) \tag{3}$$

where $\vec{F}$ is the force vector on the wire, L is the scalar length of wire in the field, $\vec{i}$ is the current vector, and $\vec{B}$ is the magnetic field vector at the location of the wire. This effect would cause the EDM wire to deflect and possibly vibrate while cutting due to the current from the discharges in the wire and the permanent magnetic field of the samples. Indications of this effect could be slow machining rates due to a high number of shorts in the wire, or larger than normal kerfs due to the wire deflecting and vibrating. For these reasons the polar direction of the magnet was included in the design of experiments.

The capacitance and the polar direction were considered ordinal factors since they are discrete values. The voltage is considered a continuous factor since the voltage on the WEDM used can be set at any value between 0-300 V. The maximum capacitance value of 22 nF was chosen because preliminary testing showed that higher values contributed to excessive wire breakage. The control factors for the DOE are listed in Table 5.2. There are only three control factors considered, therefore the "D" column in Table 5.1 will be omitted. This yields the DOE found in Table 5.3.

The DOE was performed on 9.53mm (0.375 in) NdFeB cubes of the same grade as desired for the helical prototypes (N42). Test cuts were completed by cutting deep slits halfway through the cube, near the center of the cube as shown in Figure 5.1. The wire position was sampled and recorded every second and written to a text file by the WEDM software. This information was then used to calculate the slicing rate of each cut. 100 μm diameter brass wire was used for all cuts in the experiment.

5.1.2 Taguchi Results

Each experiment was performed three times. The response factors considered were the slicing rate, which is to be maximized, and the kerf loss and variation, which are to be minimized. The signal-to-noise ratio, η(dB), which is a measure of the variation present, was calculated for each of the experiments [25]. The slicing rate signal-to-noise ratio was calculated using the "higher the better" method in equation (4) [25].

$$\eta = -10\log_{10}\left(\frac{1}{n}\sum_{i=1}^{n}\frac{1}{{y_i}^2}\right) \qquad (4)$$

where n is the number of tests in a trial and y_i is the value of the response for the given experiment trial. The results for the slicing rate experiment are found in Table 5.4. An analysis of variance (ANOVA) and F-test were performed for each of the experiments, and is found in Table 5.5.

The F ratio is the ratio of variance due to the effect of a factor and variance due to the error term [26]. Increasing F ratio corresponds to increasing significance in the model. The % contribution is the sum of the squares of the control factor divided by the total sum of the squares. The % contribution is the contribution of each factor toward the variation in the output. The Prob>F is the probability of obtaining, by chance alone, a greater F ratio if there is no difference between the sum of squares of the parameter and the sum of squares of the error. Probabilities of less than 0.05 are considered statistically significant. Table 5.5 shows that for slicing rate, the capacitance is the primary contributing factor (70%), voltage is secondary (27%), and the polar direction plays a statistically insignificant role in the variance.

Finally, the optimal levels of each parameter were determined from the mean signal to noise ratio at each control level and are shown in Table 5.6. Table 5.6shows that the highest level of voltage (300 V) and capacitance (22 nF) will maximize the slicing rate.

The kerf values were measured on an optical measurement system. Each slice was measured 20 times and the average was used for data processing. The full lists of measured values with standard deviations are contained in Appendix B. The results of the kerf measurements are tabulated in Table 5.7. The kerf loss signal to noise ratio was calculated using the “lower the better” method in equation (5) [25].

$$\eta = -10\log_{10}\left(\frac{1}{n}\sum_{i=1}^{n} y_i^{\ 2}\right) \tag{5}$$

where n is the number of tests in a trial and y_i is the value of the response for the given experiment trial. An ANOVA and F-test were performed on the kerf data, using the same procedure as the slicing rate analysis. Table 5.8 shows that the voltage is the primary contributor to variation in the kerf (97%), while capacitance and polar direction have statistically insignificant effects. This is to be expected because the driving force for a spark to occur is electric potential. Higher voltages cause the dielectric fluid to ionize over greater distances, creating a larger kerf.

The optimal levels for each of the three control factors were determined for minimizing kerf and are found in Table 5.9. It was found that, as expected, the smallest voltage tested (150 V) caused minimum kerf loss. The optimal levels for capacitance and polar direction were found, but are not considered significant since their % contribution to variance is much less than voltage and their Prob>F is much greater than 0.05. The variation in the kerf was analyzed by using the standard deviation, σ, of the measured kerf for each test cut. The variation in kerf is tabulated in Table 5.10. An ANOVA and F-test were performed on the standard deviation of the measured kerfs and is found in Table 5.11

Although the % contribution indicates that the capacitance and polar direction affect the variation in the output, the Prob>F of more than 0.05 indicates that the control factors do not affect the variation in kerf with any statistical significance.

5.1.3 Confirmation Experiments

In order to determine if interactions between the control parameters are occurring, and to assess the "goodness" of the Taguchi analysis, confirmation experiments must be completed. The predicted optimal value of the signal-to-noise ratio can be calculated as follows [24]:

$$\eta_{opt} = \eta_m + \sum_{j=1}^{k} \left(\eta_j - \eta_m\right) \qquad (6)$$

where η_{opt} is the predicted optimal SN ratio, η_m is the overall mean SN ratio, η_j is the mean SN ratio at the optimal level, and k is the number of control factors that affect the response. As shown in Table 5.6, the optimal levels for the slicing rate were $V_3C_3D_2$ where V, C, and D correspond to voltage, capacitance, and polar direction control factors, respectively, and the subscript corresponds to the level of the control factor. Table 5.12 shows that the predicted and experimental optimal SN ratios for the slicing rate are in close agreement with each other. This indicates that the model holds true and interactions between the control factors are not significant.

The optimal levels for minimizing kerf loss were $V_1C_1D_1$, as shown in Table 5.9. Table 5.13 shows that the values for the predicted and experimental SN ratios for kerf loss were also in close agreement, indicating that interactions are not likely occurring and that the model holds true. Since none of the control factors contributed to the variation in kerf with any statistical significance, a confirmation experiment was omitted for the variation in kerf.

5.1.4 Parameter Optimization Summary

Since the slicing rate is a primary factor when manufacturing helical devices, the optimal settings for the slicing rate ($V_3C_3D_2$) will be used to WEDM the devices. The increase in kerf loss between the kerf loss optimal settings ($V_1C_1D_1$), and the slicing rate optimal settings is ≈40 μm. This is considered acceptable since the overall diameter of the device is much larger at ≈3200 μm, and the kerf loss at the optimal slicing rate is known and can be accounted for.

The data also showed that the polar direction of the wire is not a significant factor for either slicing rate, kerf loss, or variation in kerf. This provides evidence that the lorentz forces on the wire due to the magnetic field and the current in the wire do not significantly affect the machining process for the NdFeB samples tested.

5.2 Magnetic Loss Due to Machining

As discussed in earlier chapters, when a magnetic material is heated above its Curie temperature, it loses its magnetization. Since at least a portion of the WEDM machined NdFeB is heated above the Curie point out of necessity for material to be removed, there is a portion of the magnet that will become demagnetized. The following experiment was used to analyze the magnetic losses in the machined magnets.

Five diametrically magnetized cylindrical magnets were machined using the WEDM. The magnets had nominal dimensions of 3.175 mm diameter and 6.350 mm length. The samples were fixtured for machining and testing by bonding them to the end of a brass dowel pin with electrically conductive adhesive as shown in Figure 5.2. This fixturing allowed for the workpiece to be held on the brass dowel pin, allowing the wire to machine the entire length of the magnet. The adhesive used was Resinlab SEC1233 silver filled epoxy with a volume resistivity of 0.003 ohm-mm. This added a negligible amount of resistance to the workpiece. The samples were placed in a magnetic field generated by a set of orthogonal Helmoltz coils designed and built under the direction of Dr. Jake Abbott in the Telerobotics Lab at the University of Utah [18]. The Helmholtz coils were controlled and data acquisition was performed with the assistance of Arthur Mahoney, a PhD candidate in the Telerobotics Lab. The samples were fixed at the end of a long shaft attached to an ATI Nano 17 [27] force-torque sensor as shown in Figure 5.3. Two constraint uprights were used to limit the maximum deflection of the shaft so the moment applied to the torque sensor could not exceed the maximum recommended value specified by the manufacturer. The uprights had an annular air gap surrounding the shaft and therefore did not contribute significant friction or resistive torque moment to the system. The samples were placed in the middle of the coils, where the field is considered uniform. The coils created a magnetic field that rotated about the axis of the cylindrical magnet. The moment from the force-torque sensor was measured at a frequency of 2 Hz. The rotating field generates a sinusoidal torque on the magnet. Five cylindrical magnets were measured with the force-torque sensor. The magnets were then machined to smaller diameters in the WEDM according to Table 5.14. The samples were then re-measured in the coils with the force-torque sensor after machining. A sample, after machining, is shown in Figure 5.4.

A field of 10.37 ± 0.05 mT was applied and rotated at a speed of 0.025 Hz (40 sec/rev). The measured torque curves were normalized and fit with a sine wave using a least-squares fitting process. Figure 5.5 through Figure 5.9 show the data acquired from the torque experiment, fit sine curves, and ± 2 standard deviation band curves. The coefficient of determination, R^2, is also shown, indicating the variance between the acquired data and the fit sine wave.

The measured amplitude of the sine wave for each of the five samples is tabulated in Table 5.15 The reduction in the magnitude of the machined samples is due to the reduction in size, change in shape anisotropy, and the demagnetized layer due to the HAZ. This reduction in measured torque was then used in a finite element analysis to determine the depth of the demagnetized layer.

5.3 Magnetic Finite Element Analysis[1]

Although a magnetic material may not have a homogeneous magnetic structure at microscopic scales, the material can be modeled as having an average magnetization across the volume. This average magnetization is a function of the shape of the material, magnetic history of the material, and the applied field; for hard-magnetic materials like NdFeB placed in a relatively weak magnetic field ($H_{Applied}$ << H_c) the average magnetization can be described by:

$$\vec{M}_{avg} = \chi \vec{H}_{\text{Internal}} + \vec{M}_r \qquad (7)$$

where χ is the susceptibility of the material, $H_{Internal}$ is the internal field, H_c is the coercive field strength required to demagnetize the permanent magnet, and M_r is the magnetic remanence, which is the shape-corrected magnetization remaining after magnet manufacturing and magnetization. The internal field is a function of the applied field and the demagnetizing field created by the magnet itself:

$$\vec{H}_{\text{Internal}} = \vec{H}_{Applied} + \vec{H}_{Demag} \qquad (8)$$

The demagnetization field is a function of geometry and material magnetization and can be written as:

$$\vec{H}_{\text{Demag}} = -N\vec{M}_{avg} \qquad (9)$$

where N is the demagnetization factor in the direction of magnetization, which is a function of geometry. Combining equations (7)-(9), the average magnetization can be described as a function of applied field and remnant magnetization by:

---

[1] *The modeling described in this section were performed by Andrew Petruska, a PhD candidate in the Telerobotics Laboratory in Department of Mechanical Engineering at the University of Utah. It is included in this thesis for completeness.*

$$\vec{M}_{avg} = \frac{1}{1+N\chi}\left(\chi\vec{H}_{\text{Applied}} + \vec{M}_r\right) \quad (10)$$

The torque experienced by the permanent magnetic material in an external field is then:

$$\vec{\tau} = \mu_0 V\left(\vec{M}_{avg} \times \vec{H}_{Applied}\right) \quad (11)$$

where V is the magnetized volume and μ_0 is permeability of free space ($4\pi \times 10^{-7}$ N/A^2), which, because any vector crossed with itself is equal to zero, reduces to:

$$\vec{\tau} = \frac{\mu_0 V}{1+N\chi}\left(\vec{M}_r \times \vec{H}_{Applied}\right) \quad (12)$$

A finite element analysis (FEA) model is created using Ansoft® Maxwell® release 14.0 software to simulate the geometry and solve equation (7) to determine the thickness of the postmachined demagnetized layer. The analysis assumes a quasistatic solution to Maxwell's electricity and magnetism equations, and a demagnetized layer of the magnet due to heating in the WEDM process. The geometry modeled is shown in Figure 5.10 and consists of a cylinder of NdFeB magnetized diametrically placed in a uniform magnetic field that is orthogonal to the remanent magnetization.

The free variables in this analysis are the demagnetized layer thickness and the remanent magnetization. The cylinder length, cylinder diameter, and applied field strength are determined by measurement. Calibration of the remanent magnetization for the analysis is performed by recognizing the linearity in equation (7) and multiplying the manufacturer-supplied remanent magnetization by the ratio of measured premachining torque to FEA-calculated torque for each sample. For these calculations the demagnetized layer thickness is taken to be zero and the overall diameter is reduced to account for the nominal plating thickness on the exterior of the magnet of 18 μm. The calculated remanent magnetization for each sample is listed in Table 5.16. The uncertainty reported includes the uncertainty in the measured torque, measured applied field, and nickel-copper-nickel plating thickness.

The demagnetized layer thickness is determined by modeling the postmachining geometries as a cylinder of magnetized NdFeB with remanent magnetization as defined by Table 5.16 surrounded by a shell of NdFeB with no remanent magnetization as shown in Figure 5.10. The diameter of the magnetized NdFeB is the measured diameter of the sample less the demagnetized layer thickness. The torque is calculated for each sample at five different demagnetized layer thicknesses. The measured torques given in Table 5.15 are then subtracted from the FEA torques calculating a modeled torque error for each sample at each demagnetization layer thickness and are plotted in Figure 5.11 along with a least-squares fit line and tolerance bands. The tolerance bands are determined by combining the uncertainties in remanent magnetization, measured torque, and measured applied field. By analyzing the zero crossing, the least-squares fit line and tolerance bands determine the demagnetized layer thickness to be 35 ± 15 µm.

5.4 Screw Designs

Several different helical device prototype designs have been machined. Torque measurements were made of the pre and postmachining torques, as described in section 5.2. Three designs are shown, along with their pre and postmachining measured torques in Figure 5.12 through Figure 5.17. The torque data show that for machined helical geometries, torque can still be generated to propel the screws.

Further designs have been proposed to more closely match the wood-screw type design, which has already been shown will work as a helical device [20]. This type of design is believed to be more able to force its way through tissue and higher viscosity fluids. An illustration of the proposed design is found in Figure 5.18.

Table 5.1- L9 Orthogonal array, adapted from Taguchi [2]

Exp. No.	A	B	C	D
1	1	1	1	1
2	1	2	2	2
3	1	3	3	3
4	2	1	2	3
5	2	2	3	1
6	2	3	1	2
7	3	1	3	2
8	3	2	1	3
9	3	3	2	1

Table 5.2- Control factors for Taguchi DOE

		Levels		
Factors	**Units**	**1**	**2**	**3**
Voltage	V	150	250	300
Capacitance	nF	3.3	10	22
Polar Direction	-	+X	+Y	+Z

Table 5.3- Taguchi DOE

Exp. No.	Voltage (V)	Capacitance (nF)	Polar Direction
1	150	3.3	+X
2	150	10	+Y
3	150	22	+Z
4	250	3.3	+Y
5	250	10	+Z
6	250	22	+X
7	300	3.3	+Z
8	300	10	+X
9	300	22	+Y

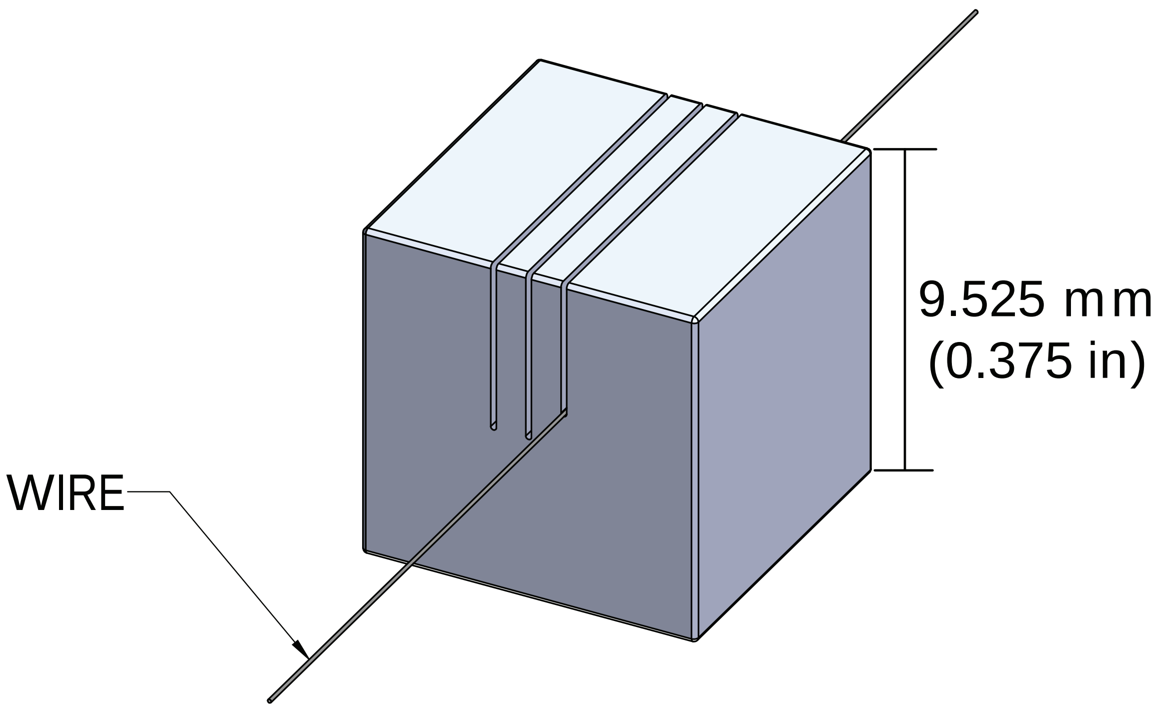

Figure 5.1- Illustration of test cuts for DOE

.

Table 5.4- Slicing rate results for DOE

Exp. No.	Voltage (V)	Capacitor (nF)	Polar Direction	Slicing Rate 1 (mm^2/min)	Slicing Rate 2 (mm^2/min)	Slicing Rate 3 (mm^2/min)	Mean (mm^2/min)	SN Ratio (dB)
1	150	3.3	+X	0.222	0.271	0.213	0.235	-12.709
2	150	10	+Y	0.442	0.438	0.433	0.438	-7.177
3	150	22	+Z	0.674	0.628	0.682	0.662	-3.607
4	250	3.3	+Y	0.418	0.446	0.445	0.436	-7.217
5	250	10	+Z	0.687	0.636	0.616	0.646	-3.818
6	250	22	+X	0.929	1.067	0.953	0.983	-0.196
7	300	3.3	+Z	0.433	0.469	0.409	0.437	-7.225
8	300	10	+X	0.677	0.778	0.641	0.699	-3.201
9	300	22	+Y	1.223	1.353	1.256	1.277	2.101

Table 5.5- ANOVA and F-test for slicing rate

Control Factor	Degree of Freedom	Sum of Squares	F ratio	Prob>F	% contribution
Voltage	1	42.218	120.728	0.0016	27.468%
Capacitance	2	107.963	154.368	0.0009	70.243%
Polar Direction	2	2.469	3.531	0.1628	1.606%
Error	3	1.049	-		0.683%
Total	8	153.699	-		100.000%

Table 5.6- Mean SN ratio at each level.
The optimal levels for slicing rate maximize the SN ratio.

	Level 1 (dB)	Level 2 (dB)	Level 3 (dB)	Optimal Level
Voltage	-7.831	-3.744	-2.775	Level 3 (300 V)
Capacitance	-9.050	-4.732	-0.567	Level 3 (22 nF)
Polar Direction	-5.369	-4.098	-4.883	Level 2 (+Y)

Table 5.7- Kerf value results for DOE

Exp. No.	Voltage (V)	Capacitor (nF)	Polar Direction	Kerf 1 (µm)	Kerf 2 (µm)	Kerf 3 (µm)	Mean (µm)	SN Ratio (dB)
1	150	3.3	+X	138.7	134.6	132.9	135.4	-42.634
2	150	10	+Y	137.1	134	135.2	135.4	-42.635
3	150	22	+Z	131.6	133.6	134.8	133.3	-42.499
4	250	3.3	+Y	152.5	156.8	156.8	155.4	-43.828
5	250	10	+Z	156.8	158.6	156.9	157.4	-43.942
6	250	22	+X	153.7	153.8	155.5	154.3	-43.769
7	300	3.3	+Z	163.2	163.2	162.3	162.9	-44.238
8	300	10	+X	162.2	161.1	163.8	162.4	-44.210
9	300	22	+Y	169.9	169.2	170.7	169.9	-44.606

Table 5.8- ANOVA and F-test for kerf

Control Factor	Degree of Freedom	Sum of Squares	F ratio	Prob>F	% contribution
Voltage	1	4.927	159.471	0.0011	97.275%
Capacitance	2	0.005	0.082	0.9235	0.100%
Polar Direction	2	0.040	0.652	0.5819	0.796%
Error	3	0.093	-		1.830%
Total	8	5.065	-		100.000%

Table 5.9- Mean SN ratio at each level. The optimal levels for kerf maximize the SN ratio.

	Level 1 (dB)	Level 2 (dB)	Level 3 (dB)	Optimum Level
Voltage	-42.589	-43.846	-44.351	Level 1 (150 V)
Capacitance	-43.567	-43.596	-43.625	Level 1 (3.3 nF)
Polar Direction	-43.538	-43.689	-43.560	Level 1 (+X)

Table 5.10 – Kerf variation results for DOE

Exp. No.	Voltage (V)	Capacitor (nF)	Polar Direction	Kerf 1 σ (μm)	Kerf 2 σ (μm)	Kerf 3 σ (μm)	Mean σ (μm)	SN Ratio (dB)
1	150	3.3	+X	2.5	1.2	2.9	2.2	-7.297
2	150	10	+Y	2.7	2.5	1.9	2.4	-7.571
3	150	22	+Z	2.3	2.2	2.2	2.2	-6.981
4	250	3.3	+Y	2.4	1.4	1.6	1.8	-5.349
5	250	10	+Z	1.6	2.6	1.4	1.9	-5.752
6	250	22	+X	2.2	3.1	1.9	2.4	-7.796
7	300	3.3	+Z	2.0	2.2	1.1	1.8	-5.250
8	300	10	+X	1.8	2.0	2.0	1.9	-5.736
9	300	22	+Y	3.0	3.1	3.1	3.1	-9.734

Table 5.11- ANOVA and F-test for kerf standard deviations

Control Factor	Degree of Freedom	Sum of Squares	F ratio	Prob>F	% contribution
Voltage	1	0.442	0.279	0.6339	2.571%
Capacitance	2	8.315	2.623	0.2194	48.324%
Polar Direction	2	3.695	1.166	0.4221	21.472%
Error	3	4.755	-		27.633%
Total	8	17.206	-		100.000%

Table 5.12- Confirmation experiment results for slicing rate

η_{opt} Predicted (dB)	η_{opt} Experimantal (dB)	% Error
2.127	2.101	1.208%

Table 5.13- Confirmation experiment results for kerf loss

η_{opt} Predicted (dB)	η_{opt} Experimantal (dB)	% Error
-42.503	-42.634	0.308%

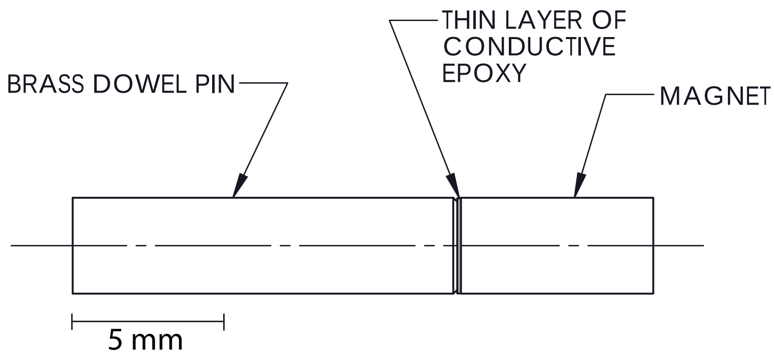

Figure 5.2- Specimen for machining in rotary table

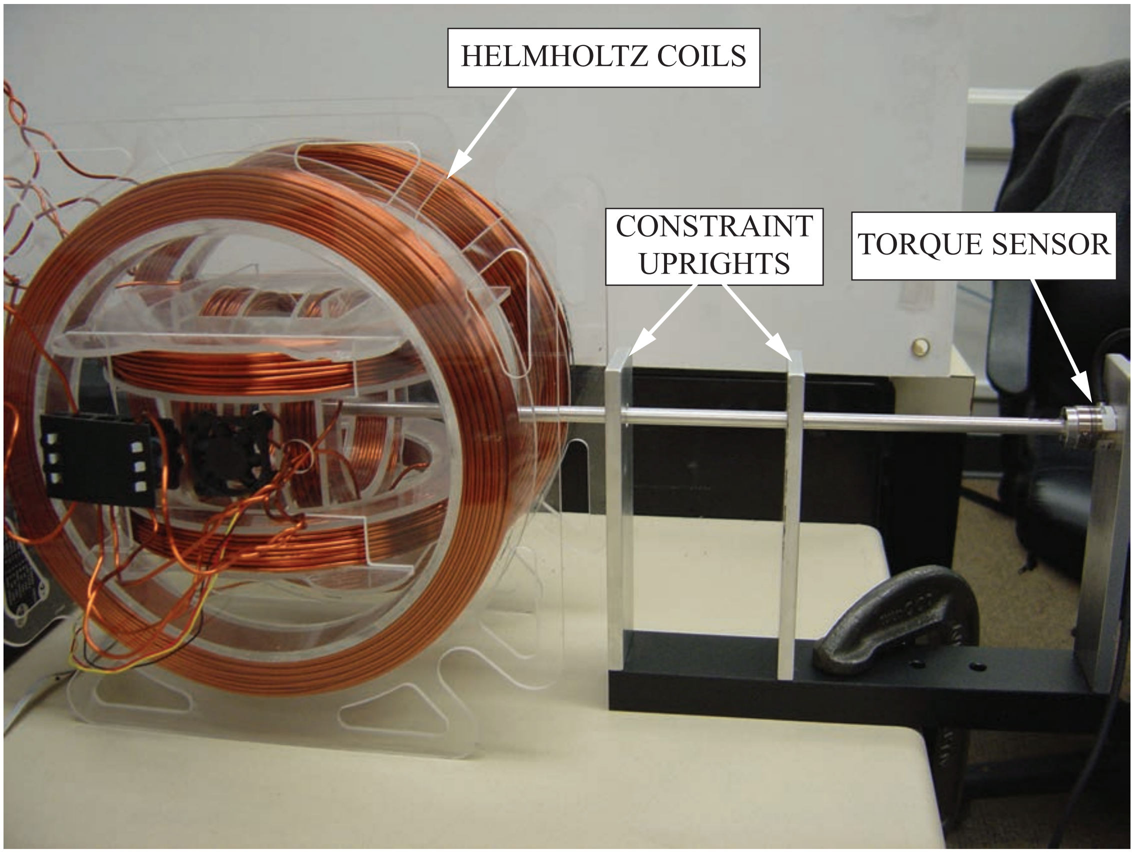

Figure 5.3- Setup for torque measurements

Table 5.14- Diameters of torque testing samples

Sample Number	Premachined Ø (mm ± 1 μm)	Postmachined Ø (mm ± 1 μm)	Length (mm ± 1 μm)
1	3.150	2.805	6.351
2	3.157	2.532	6.351
3	3.134	2.300	6.327
4	3.141	1.979	6.344
5	3.150	1.631	6.344

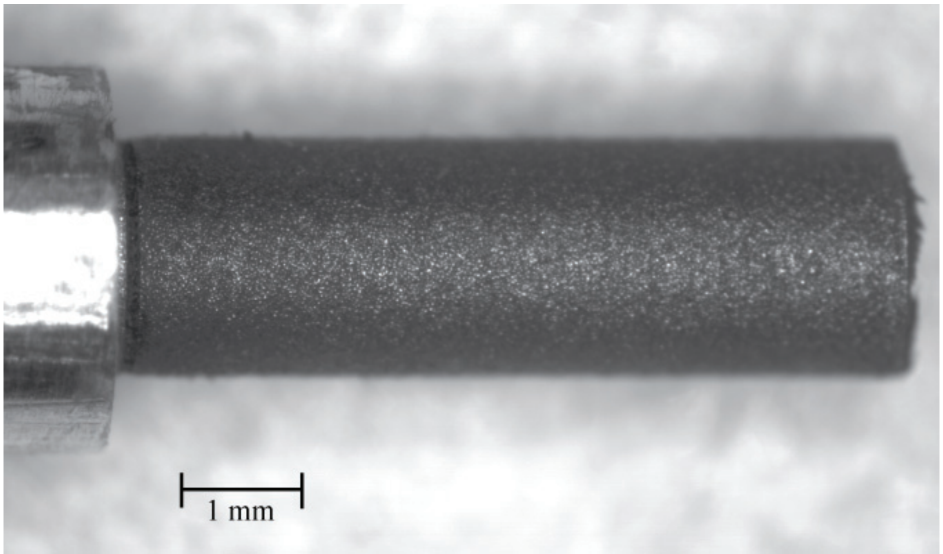

Figure 5.4- Machined sample for torque testing

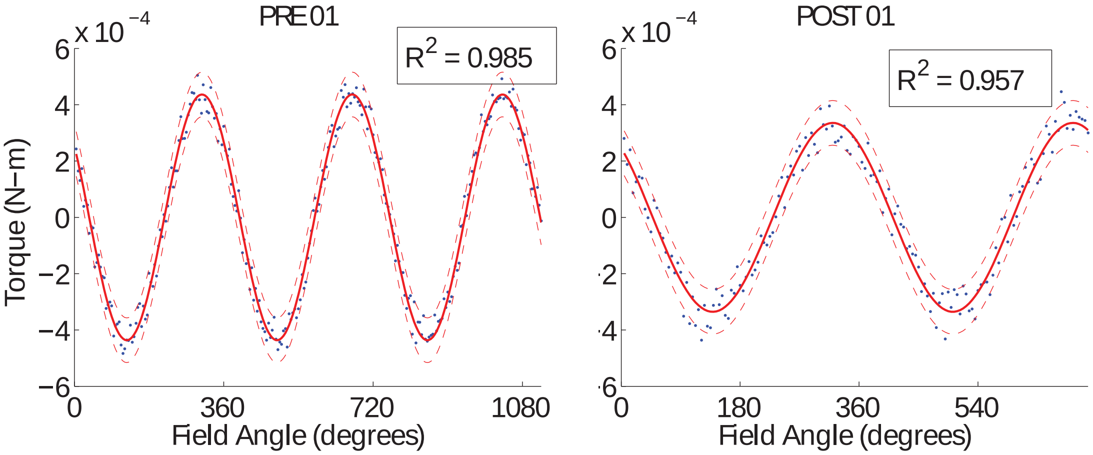

Figure 5.5- Pre- and postmachined measured torques for sample 1

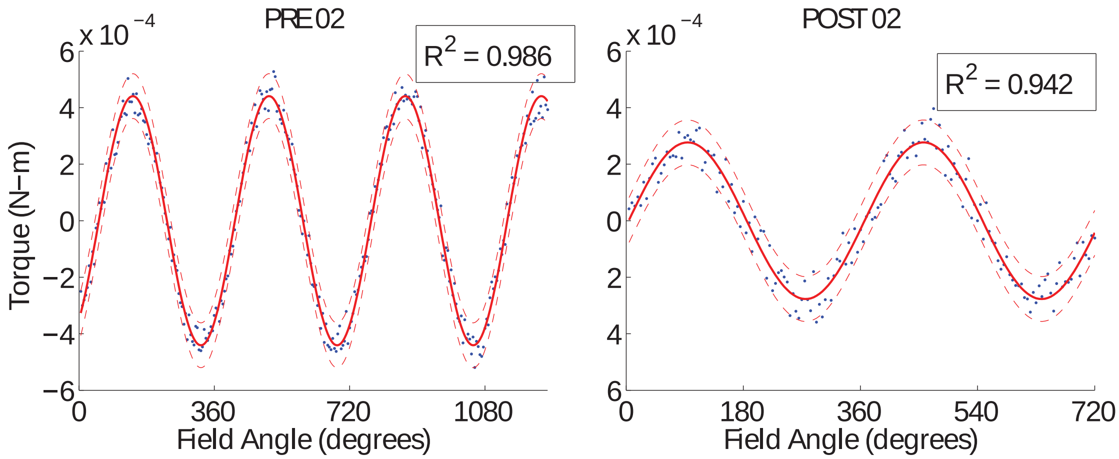

Figure 5.6- Pre- and postmachined measured torques for sample 2

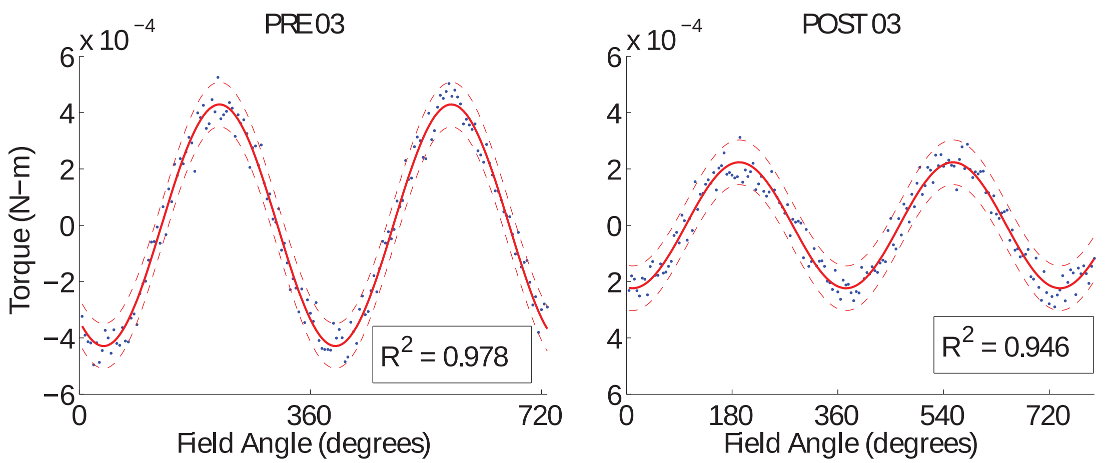

Figure 5.7- Pre- and postmachined measured torques for sample 3

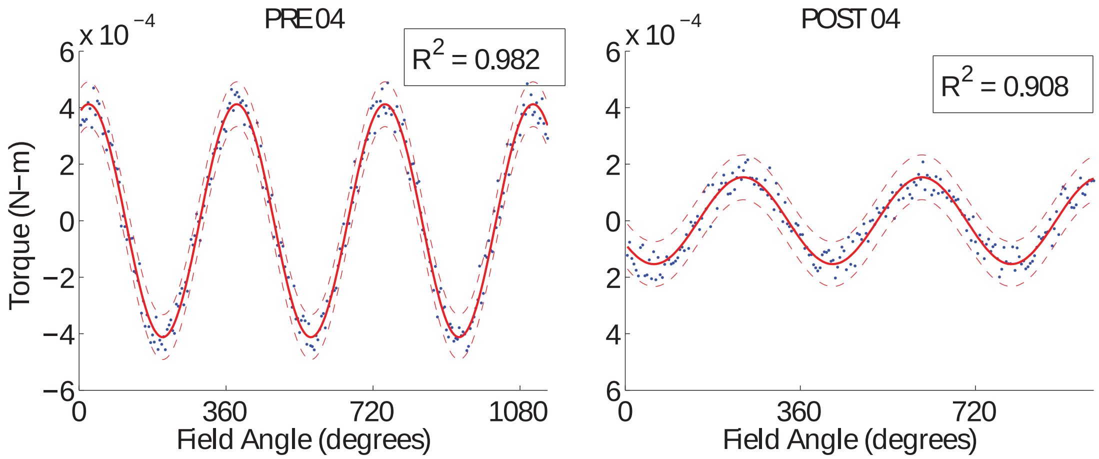

Figure 5.8- Pre- and postmachined measured torques for sample 4

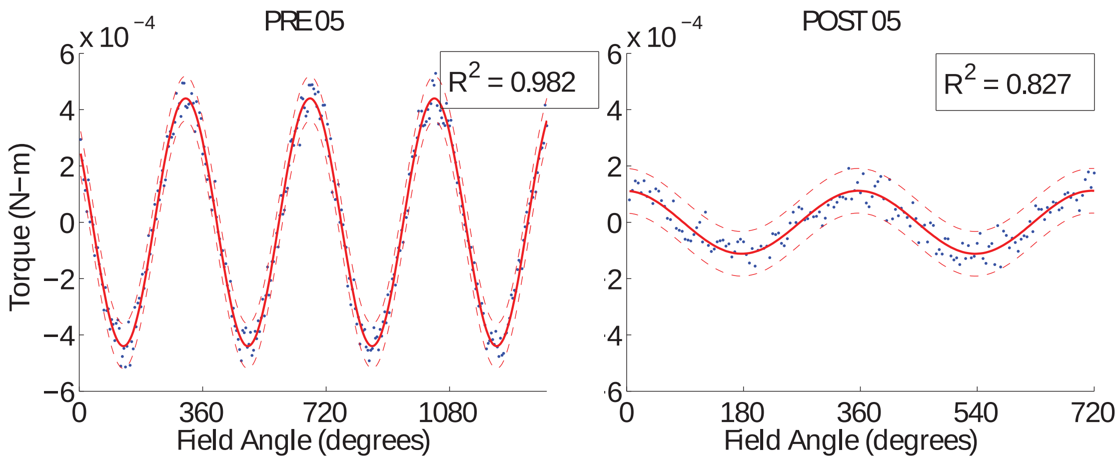

Figure 5.9- Pre- and postmachined measured torques for sample 5

Table 5.15- Measured torque values with uncertainty

Sample Number	Premachined Torque (10^{-3} N-m)	Postmachined Torque (10^{-3} N-m)
1	0.4364 ± 0.0103	0.3354 ± 0.0108
2	0.4410 ± 0.0102	0.2772 ± 0.0107
3	0.4291 ± 0.0106	0.2237 ± 0.0104
4	0.4123 ± 0.0103	0.1537 ± 0.0103
5	0.4400 ± 0.0103	0.1119 ± 0.0104

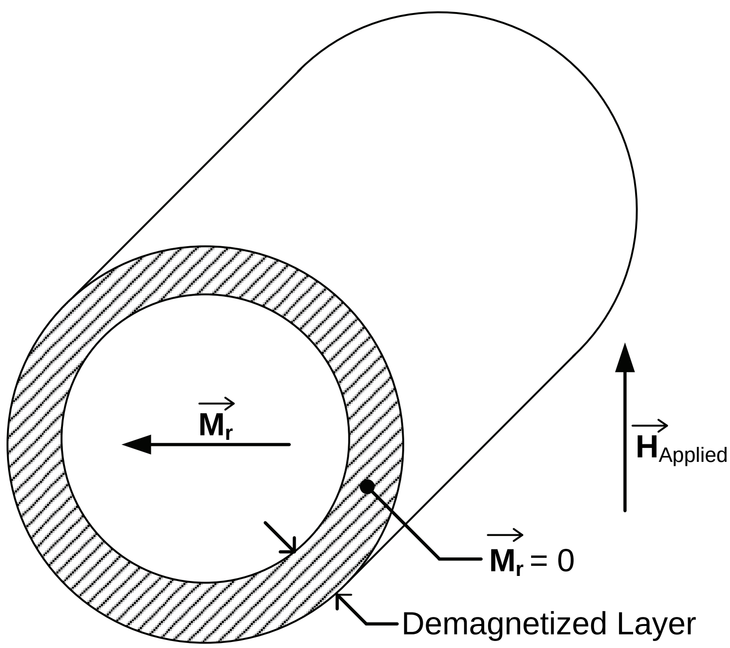

Figure 5.10- FEA modeled geometry

Table 5.16- Sample Remanent Magnetization

Sample Number	Remanent Magnetization (10^3 A/m)
1	859.5 ± 22.7
2	864.3 ± 22.9
3	855.8 ± 24.3
4	817.8 ± 21.0
5	866.9 ± 22.9

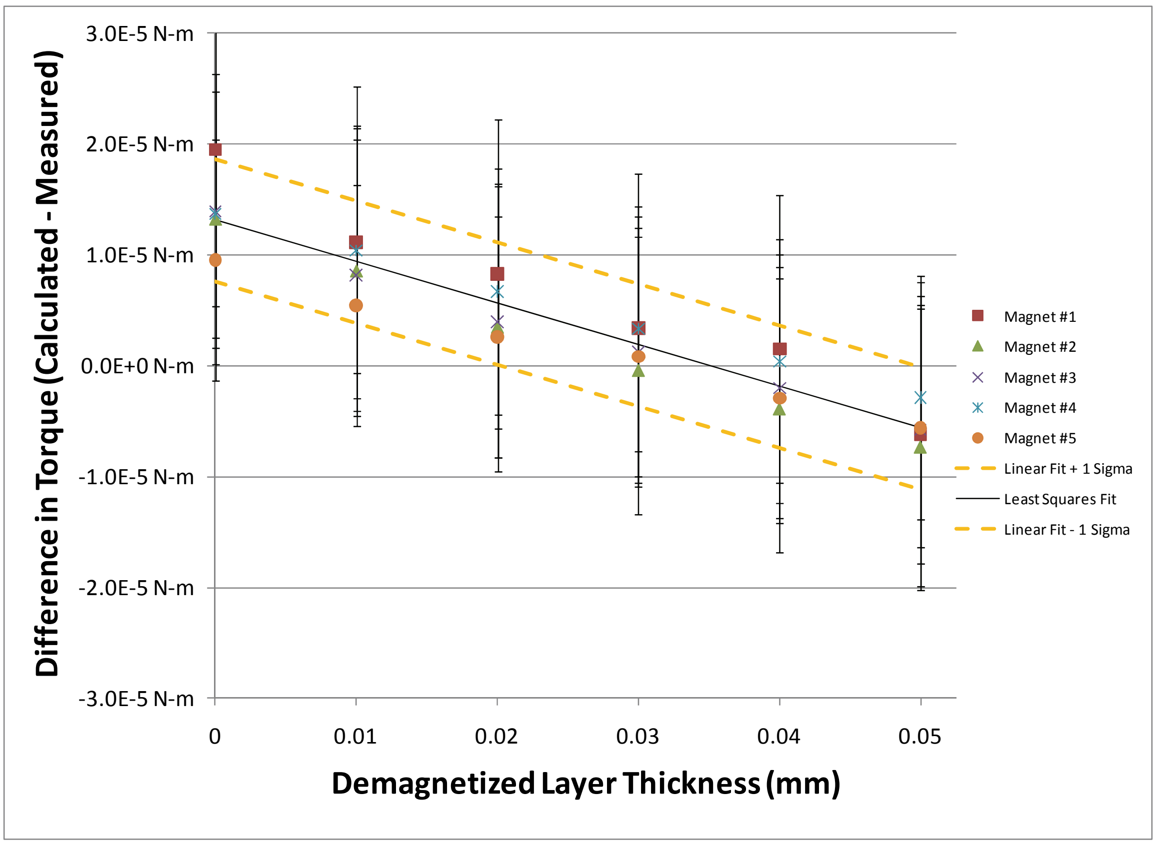

Figure 5.11- Demagnetized Layer Thickness Analysis Results

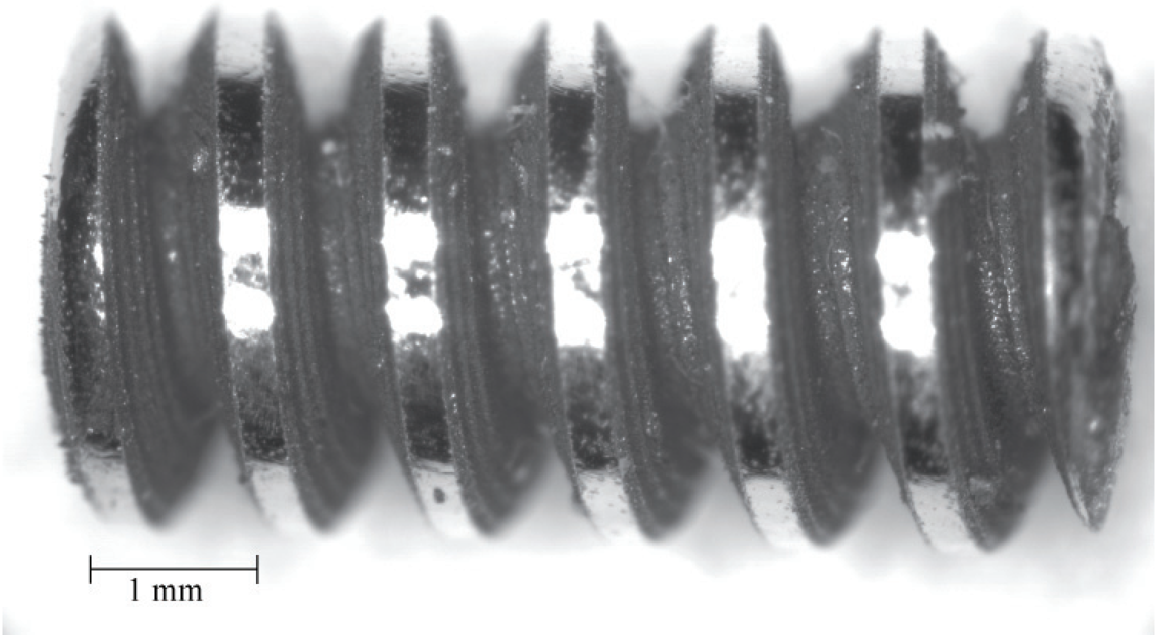

Figure 5.12- Screw prototype A

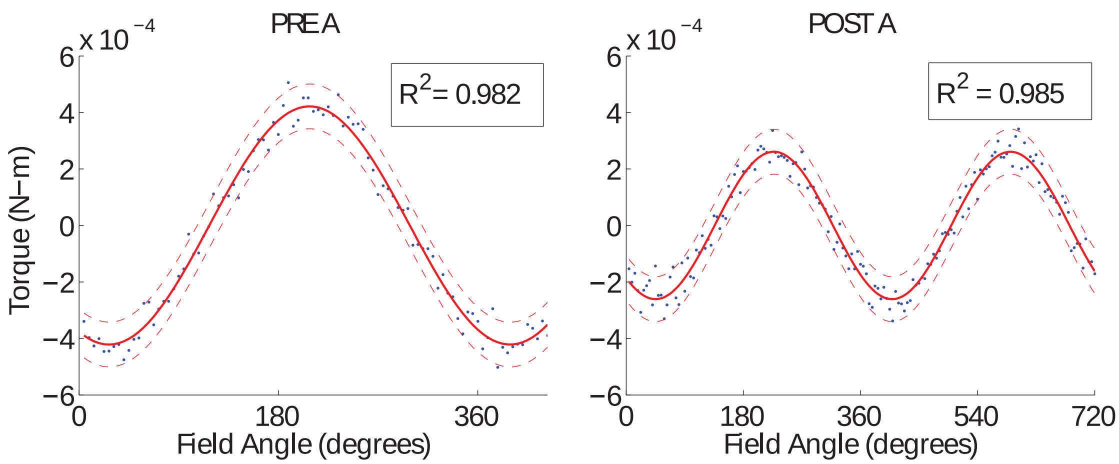

Figure 5.13- Pre- and postmachining measured torques for screw prototype A

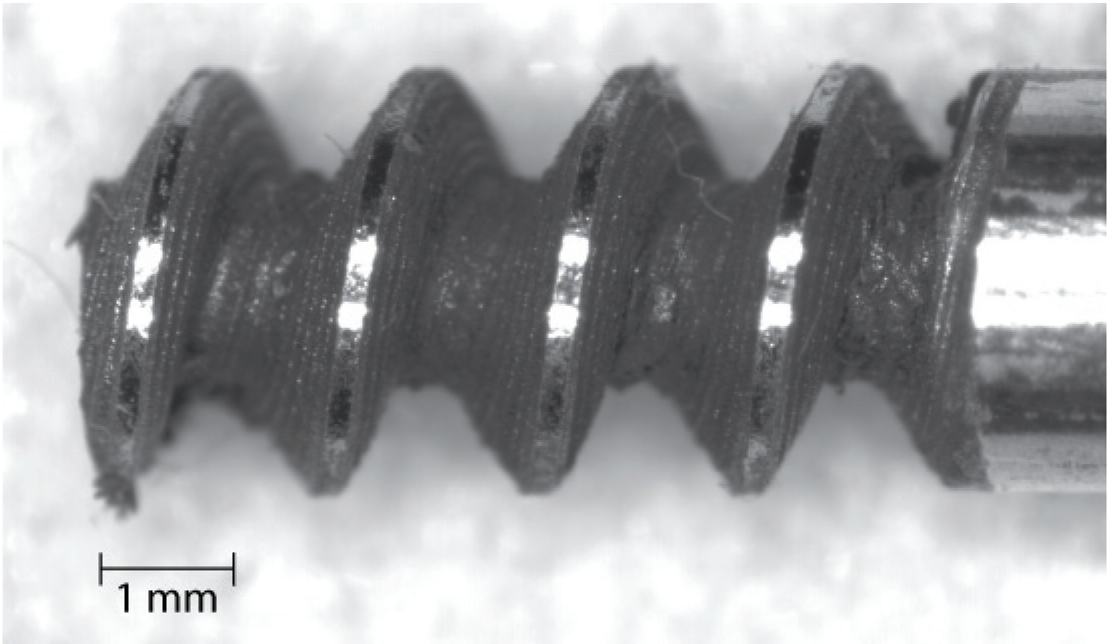

Figure 5.14- Screw prototype B

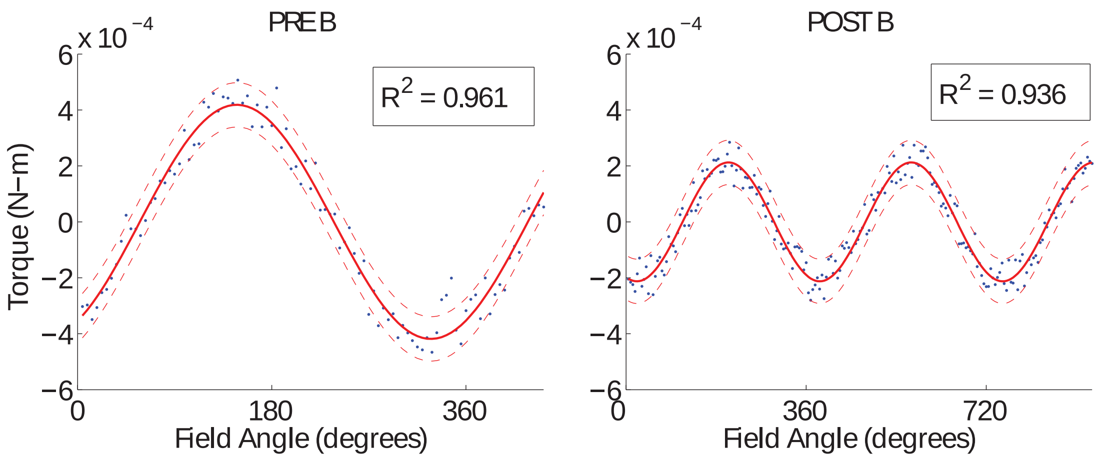

Figure 5.15- Pre- and postmachining measured torques for screw prototype B

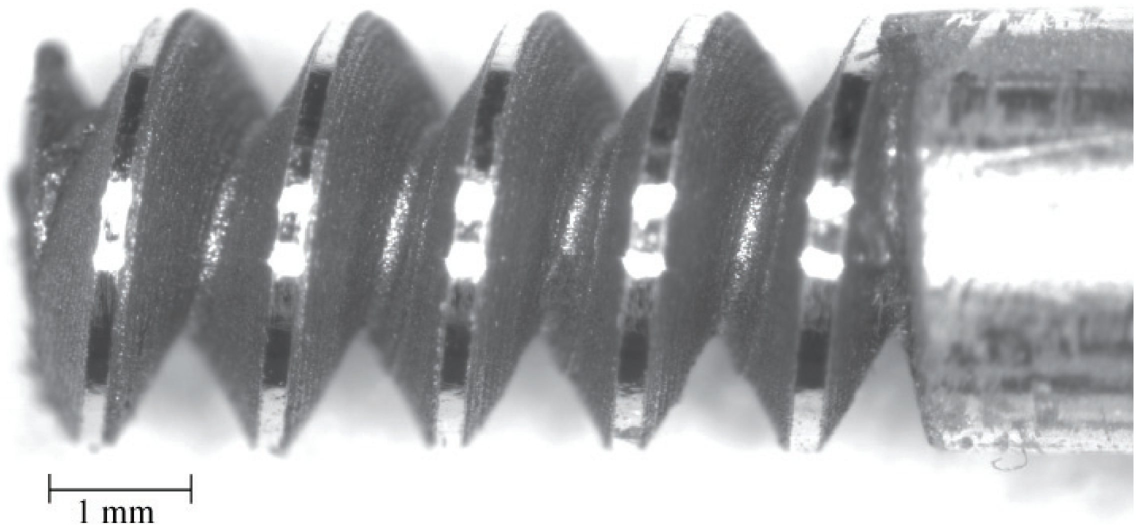

Figure 5.16- Screw prototype C

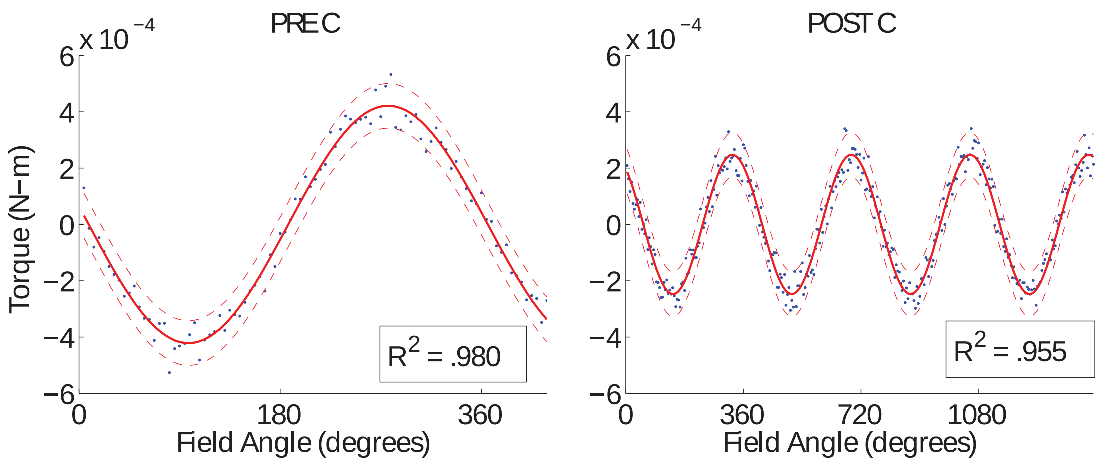

Figure 5.17- Pre- and postmachining measured torques for screw prototype C

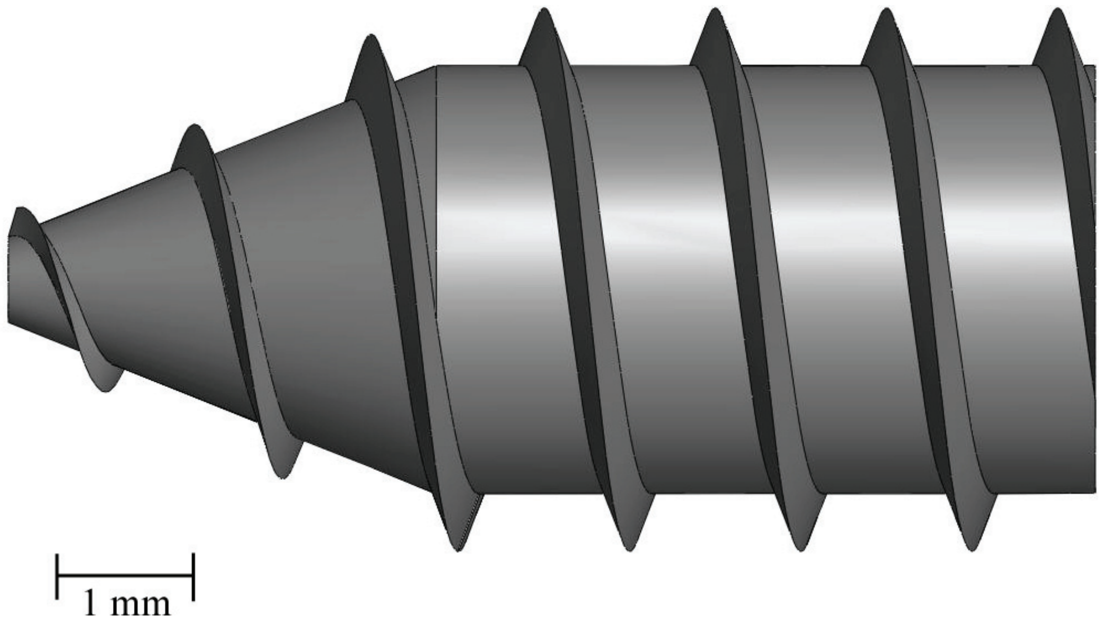

Figure 5.18- Proposed NdFeB magnet screw design

6 CONCLUSIONS AND FUTURE WORK

6.1 Conclusions

The purpose of this research was to develop a magnetic helical device. This was done by developing a fabrication method on a WEDM, optimizing the WEDM parameters, and analyzing the loss of magnetism in the machined magnets.

It was found that by altering the angle of the rotational axis of the WEDM with respect to the wire, helical geometries could be cut. A small amount of error, namely overcut in the threads, was created because of the limited number of axis of the WEDM used. This error was acceptable and was deemed small (<0.010mm) when compared with the overall diameter of the screw (3.175mm).

The optimal cutting parameters for the WEDM were found by utilizing a Taguchi design of experiments. It was found that increasing levels of voltage and capacitance increased the slicing rate, and that the polar direction of the magnet contributed an insignificant amount (1.6%) to the variation in the slicing rate. Decreasing voltage decreased the size of the kerf machined by the WEDM, whereas capacitance and polar direction contributed insignificant amounts to the variation in kerf, 0.1% and 0.8%, respectively.

A finite element analysis was performed to analyze the depth of the demagnetized layer from heating effects from the WEDM. This analysis found that the loss of magnetic field in the HAZ was 35 ± 15 μm for the cylindrical magnets tested. This depth of demagnetized skin is relatively small when considering the overall diameter of the cylindrical magnets, but would become more significant as the diameter of the screw device is decreased.

One aspect that inhibited optimal machining of the magnet workpieces was that the machined particles adhered to the part. Jet flushing enhanced the removal of these particles, but did not solve the problem completely. The adhered particles contributed to and increased number of shorts detected by the machine and increased machining times. Furthermore, when attempting to remove the wire from deep machined slots, the wire would wedge in the particles and often break. The particles were best removed postmachining with compressed air, although this may break brittle workpieces, such as NdFeB magnets.

6.2 Future Work

Further analysis could be done to measure and analyze the HAZ of the machined magnets. Typically this is done using a scanning electron microscope (SEM), but this can be difficult for permanent-magnetic materials. Machined particles adhere to the part and are difficult to fully remove. These particles could do damage to the SEM. The magnetic fields also may pose a problem, although images have been obtained in a SEM and a transmission electron microscope (TEM) [1,28].

Because the machined particles adhere to the workpiece and inhibit flushing, it may be desirable to machine the magnets premagnetization. This would eliminate particles adhering to the workpiece, improve flushing, and negate any loss of permanent magnetism due to heating of the workpiece. If desired, the HAZ could also be etched off and protective plating could be applied to the machined surfaces prior to magnetization.

Other fabrication methods could also be investigated. The helical devices could be sintered net shape. A complicated mold would need to be fabricated. This would allow for easier mass manufacture and less cost for the consumer. Because of the brittle nature of NdFeB, any postsintering shaping process, including EDM, is bound to be relatively slow and costly compared to sintering the magnet net shape.

The helical devices manufactured are a relatively complex shape. Because of this, they may exhibit a high degree of shape anisotropy, where the shape of the magnet plays a role in the permanent magnetic field. Further analysis, such as finite element analysis, could be performed to better characterize the field of the devices. This could improve understanding of the magnets behavior when an external field is applied, and may aid in controlling the device.

The helical devices described in this work could be investigated for use in hyperthermia or thermoablation. As previously discussed, raising the local temperature of tissue is one method of treating cancerous tissue. Hyperthermia takes place at 40-50°C, and thermoablation takes place over 50°C [29]. The maximum working temperature of the magnets used for this work is specified by the supplier as 80°C. Heat can be applied to the magnets externally through inductive methods. As long as the magnet was uniformly heated and the temperature was kept below the maximum working temperature, the device could be used for local heating and then extracted. If the device material was biocompatible, the device could be raised to any temperature and left in place if the Curie temperature was exceeded. Further work could also be done by attaching a different material to the magnet and have the induction circuit tuned to heat that material more than the permanent magnet.

APPENDIX A

MATLAB CODE

```
% gcode.m
% will write g code
% Author: Jeremy Greer

% Description:
% This will write a gcode file for the cutting of a helical geometry on
the
% WEDM.  The data points are input in the chart below in the order to
be
% machined.
% Generally a "key file" is advantageous for use when the wire breaks
etc.
% This can be created by specifiying a filename, ie 07key.gcf and
% UN-commenting the lines below that state:
% % toggle comment this line "key"
% For general use these lines should remain commented out.


clear
% (row,col) matlab syntax

filename = '07.gcf'; % name.ext for gcode (gcf file)

%pt     Y_start   Z     Y_end       deg rotation
data = {...
'A'     0.000   1.595   -6.244      -1799.7
'X'     0.896   1.595   -6.244      -2058.0
'B'     0.039   1.525   -6.244      -1811.0
'W'     0.857   1.525   -6.244      -2046.7
'C'     0.077   1.455   -6.244      -1821.9
'V'     0.819   1.455   -6.244      -2035.8
'D'     0.116   1.385   -6.244      -1833.1
'U'     0.78    1.385   -6.244      -2024.5
'E'     0.155   1.315   -6.244      -1844.4
'T'     0.741   1.315   -6.244      -2013.3
'F'     0.194   1.246   -6.244      -1855.6
'S'     0.702   1.246   -6.244      -2002.0
'G'     0.233   1.176   -6.244      -1866.9
```

```
'R'     0.663   1.176   -6.244      -1990.8
'H'     0.272   1.106   -6.244      -1878.1
'Q'     0.624   1.106   -6.244      -1979.6
'I'     0.312   1.036   -6.244      -1889.6
'P'     0.584   1.036   -6.244      -1968.0
'J'     0.351   0.967   -6.244      -1900.9
'O'     0.545   0.967   -6.244      -1956.8
'K'     0.391   0.898   -6.244      -1912.4
'N'     0.504   0.898   -6.244      -1945.0
'L'     0.432   0.829   -6.244      -1924.2
'M'     0.464   0.829   -6.244      -1933.5;};
name     = char(data(:,1));
Y_start  = cell2mat(data(:,2));
Z_height = cell2mat(data(:,3));
Y_end    = cell2mat(data(:,4));
rot      = cell2mat(data(:,5));

%%%%%% General outline for G code generation
% G45 H300 T4
% G01 YSTART Z1.75 F2.0
% ZHEIGHT F0.2
% YEND BDEG ROT F0.50
% Z1.8 F0.01             This is slow rise out of cut to prevent wire
break
% Z5.0 F1.0
% B0.0 F15.0             "re-winds rotary axis
% Y1.0 F1.0
% %%%%%%%REPEAT
% G01......
%fprintf(fid, '%6.2f %12.8f\n', y);



fid = fopen(filename,'w');
fprintf(fid,'G45 H300 T4\n')            % input voltage and capacitor
for i = 1:length(name)
% fprintf(fid,'\n')                      % toggle comment this line
"key"
% fprintf(fid,'%s\n',char(name(i,:)))    % toggle comment this line
"key"
fprintf(fid,'G01 Y%0.3f Z1.75 F2.0\n',Y_start(i))
fprintf(fid,'Z%0.3f F0.2\n',Z_height(i))
fprintf(fid,'Y%0.3f B%0.1f F0.50\n',Y_end(i),rot(i))
fprintf(fid,'Z1.8 F0.01\n')
fprintf(fid,'Z5.0 F1.0\n')
fprintf(fid,'B0.0 F15.0\n')
fprintf(fid,'Y1.0 F1.0\n')
end
%fprintf(fid,'\n')                       % toggle comment this line
"key"
fprintf(fid,'M30')
fclose(fid);
```

APPENDIX B

KERF MEASUREMENTS

Table 0.1- Kerf measurements for test cut samples 1 and 2

	150V 3.3nF PX				150V 10nF PY		
	1	2	3		1	2	3
1	137.201	133.398	133.971	1	131.327	131.687	135.413
2	138.135	133.123	133.512	2	136.590	131.221	134.027
3	141.231	134.565	135.485	3	138.561	130.948	134.781
4	142.220	136.024	135.234	4	139.967	136.257	137.312
5	141.451	137.595	134.844	5	142.295	138.396	138.528
6	141.886	135.137	129.196	6	141.137	138.068	140.845
7	143.424	135.063	128.690	7	139.522	135.135	135.239
8	138.819	134.939	128.330	8	137.410	135.767	134.245
9	140.677	133.502	127.287	9	137.551	135.333	135.394
10	136.180	133.477	129.996	10	133.140	133.440	135.054
11	137.167	133.641	130.555	11	136.639	133.194	134.926
12	141.111	136.087	135.019	12	138.022	136.571	132.867
13	136.431	136.336	132.328	13	137.053	135.113	136.303
14	135.843	133.626	133.359	14	137.178	131.521	134.044
15	134.569	134.460	135.411	15	136.839	128.994	133.982
16	137.235	135.156	131.179	16	136.050	133.407	133.592
17	139.822	133.241	135.241	17	137.866	135.681	134.116
18	136.653	133.253	135.300	18	134.649	134.321	135.177
19	136.819	134.529	135.943	19	136.377	131.946	133.686
20	137.958	135.363	136.813	20	133.067	132.228	134.609
mean	**138.7**	**134.6**	**132.9**	**mean**	**137.1**	**134.0**	**135.2**
stdev	**2.5**	**1.2**	**2.9**	**stdev**	**2.7**	**2.5**	**1.9**

Table 0.2- Kerf measurements for test cut samples 3 and 4

	150V 22nF PZ		
	1	2	3
1	127.865	129.135	134.963
2	129.018	135.248	134.490
3	131.738	133.037	138.395
4	133.124	131.525	137.338
5	128.306	131.354	131.378
6	129.161	134.238	131.100
7	129.734	134.009	134.016
8	132.426	133.922	133.939
9	129.088	136.446	131.943
10	129.257	133.153	136.306
11	130.262	132.709	136.214
12	133.865	133.278	137.287
13	134.460	131.595	138.006
14	133.999	137.324	134.626
15	134.610	135.819	136.448
16	132.370	132.000	132.385
17	132.466	132.819	132.068
18	134.250	137.984	135.055
19	134.097	132.704	133.956
20	132.796	133.755	135.732
mean	**131.6**	**133.6**	**134.8**
stdev	**2.3**	**2.2**	**2.2**

	250V 3.3nF PY		
	1	2	3
1	152.284	152.808	153.461
2	153.408	155.708	153.854
3	154.367	156.999	157.991
4	153.882	158.495	156.820
5	152.180	158.935	159.548
6	155.757	158.132	159.647
7	154.804	156.886	159.176
8	154.339	157.543	156.118
9	154.367	156.493	156.250
10	152.021	156.120	155.961
11	151.905	155.864	156.459
12	151.548	157.337	156.073
13	151.461	157.136	156.394
14	153.040	156.694	156.670
15	149.710	156.353	158.520
16	145.200	157.316	155.965
17	148.747	158.187	157.199
18	153.785	154.484	156.066
19	152.837	157.087	156.193
20	153.964	157.204	158.012
mean	**152.5**	**156.8**	**156.8**
stdev	**2.4**	**1.4**	**1.6**

Table 0.3- Kerf measurements for test cut samples 5 and 6

	250V 10nF PZ				250V 22nF PX		
	1	2	3		1	2	3
1	157.577	160.251	155.826	1	153.275	152.268	153.887
2	158.122	161.501	154.474	2	154.405	155.420	155.425
3	156.146	156.760	157.787	3	155.626	153.823	155.202
4	155.480	157.242	158.066	4	155.888	155.267	158.431
5	157.583	158.541	157.172	5	156.955	157.279	155.596
6	157.085	159.930	157.684	6	153.450	154.809	158.832
7	154.694	160.431	158.274	7	155.098	155.801	154.714
8	156.517	166.067	157.081	8	155.193	158.849	156.948
9	156.050	159.095	157.284	9	156.360	155.911	154.686
10	156.954	154.777	158.899	10	158.003	146.652	155.924
11	156.083	154.401	158.685	11	153.089	155.286	156.886
12	155.524	157.537	157.281	12	152.088	155.193	157.188
13	153.548	159.555	154.553	13	151.117	150.601	152.543
14	157.451	160.290	158.077	14	151.015	155.052	156.417
15	156.465	155.331	156.266	15	151.301	153.042	151.780
16	160.079	156.120	154.633	16	153.643	149.029	152.964
17	157.404	157.688	156.028	17	150.796	151.796	154.814
18	160.086	158.655	155.900	18	151.654	151.559	153.359
19	157.459	158.420	155.761	19	151.501	157.450	156.875
20	156.094	158.727	157.354	20	153.890	150.536	157.555
mean	**156.8**	**158.6**	**156.9**	**mean**	**153.7**	**153.8**	**155.5**
stdev	**1.6**	**2.6**	**1.4**	**stdev**	**2.2**	**3.1**	**1.9**

Table 0.4- Kerf measurements for test cut samples 7 and 8

	300V 3.3nF PZ				300V 10nF PX		
	1	2	3		1	2	3
1	160.214	160.919	159.402	1	157.826	156.928	162.046
2	164.930	163.354	161.238	2	160.710	157.829	161.439
3	168.230	163.656	162.362	3	162.651	159.486	162.433
4	166.131	162.980	163.395	4	161.107	162.210	160.964
5	163.143	163.628	160.363	5	160.705	160.142	160.845
6	164.139	166.331	163.254	6	162.894	160.448	160.980
7	164.829	163.673	162.697	7	161.945	160.183	163.923
8	163.944	162.456	162.277	8	161.286	159.823	163.465
9	162.417	162.886	163.571	9	162.697	158.547	165.533
10	160.892	163.448	161.298	10	163.063	161.325	165.364
11	161.073	162.550	162.622	11	162.292	161.876	164.199
12	163.179	159.941	162.973	12	162.585	164.752	162.565
13	164.054	159.417	162.962	13	162.546	164.073	167.138
14	161.634	159.241	162.584	14	161.660	162.700	166.341
15	160.994	163.538	163.036	15	160.194	162.999	166.754
16	163.147	163.280	162.730	16	163.533	161.302	165.543
17	163.628	164.125	162.179	17	162.504	162.033	164.080
18	162.449	164.711	161.890	18	166.793	160.960	164.664
19	161.280	165.931	161.819	19	164.376	163.490	163.973
20	163.971	167.848	163.540	20	162.864	160.252	163.623
mean	**163.2**	**163.2**	**162.3**	**mean**	**162.2**	**161.1**	**163.8**
stdev	**2.0**	**2.2**	**1.1**	**stdev**	**1.8**	**2.0**	**2.0**

Table 0.5- Kerf measurements for test cut sample 9

300V 22nF PY

	1	2	3
1	163.411	169.237	168.696
2	164.851	170.574	166.644
3	166.818	163.206	167.972
4	165.986	167.013	170.673
5	167.317	170.690	169.507
6	169.976	168.297	168.100
7	168.772	170.974	172.243
8	171.950	164.623	172.040
9	170.315	164.271	168.769
10	169.301	168.374	171.280
11	168.329	165.408	171.173
12	171.170	167.608	170.100
13	172.066	169.784	170.729
14	171.380	174.628	174.561
15	171.019	170.267	165.810
16	173.076	172.995	166.728
17	173.100	172.470	176.140
18	174.297	172.297	172.843
19	171.824	171.340	177.237
20	172.074	170.494	172.194
mean	**169.9**	**169.2**	**170.7**
stdev	**3.0**	**3.1**	**3.1**

REFERENCES

[1] Kruusing A., Leppävuori S., Uusimäki A., Petrêtis B., and Makarova O., 1999, "Micromachining of magnetic materials," Sensors and Actuators A: Physical, **74**(1-3), pp. 45-51.

[2] Taguchi G., 1987, The System of Experimental Design: Engineering Methods to Optimize Quality and Minimize Costs, UNIPUB/Kraus International Publications, White Plains New York.

[3] Campbell P., 1994, Permanent Magnet Materials and their Application, Cambridge University Press.

[4] Coey J. M. D., 1996, Rare-Earth Iron Permanent Magnets, Oxford University Press, USA.

[5] Cheng X., Wang Z. G., Kobayashi S., Nakamoto K., and Yamazaki K., 2009, "Development of a six-axis wire electrical discharge machine for the fabrication of micro end mills," Proceedings of the Institution of Mechanical Engineers, Part B: Journal of Engineering Manufacture, **223**(2), pp. 121-131.

[6] Nelson B. J., Kaliakatsos I. K., and Abbott J. J., 2010, "Microrobots for Minimally Invasive Medicine," Annu. Rev. Biomed. Eng., **12**(1), pp. 55-85.

[7] Kummer M. P., Abbott J. J., Kratochvil B. E., Borer R., Sengul A., and Nelson B. J., 2010, "OctoMag: An Electromagnetic System for 5-DOF Wireless Micromanipulation," IEEE Transactions on Robotics, **26**(6), pp. 1006-1017.

[8] K & J Magnetics, 2011, "Neodymium Magnet Physical Properties," http://www.kjmagnetics.com/specs.asp.

[9] Sagawa M., Hirosawa S., Yamamoto H., Fujimura S., and Matsuura Y., 1987, "Nd-Fe-B permanent magnet materials," Japanese Journal of Applied Physics, **26**(6), pp. 785–800.

[10] Luo N., Zhang N., and Graham C. D., 1987, "Variation of hardness with temperature in sintered NdFeB magnets," Thirty-First Annual Conference on Magnetism and Magnetic Materials, 17-20 Nov. 1986, USA, pp. 3442-3444.

[11] Stadelmaier H. H., Elmasry N. A., Liu N. C., and Cheng S. F., 1984, “The metallurgy of the iron-neodymium-boron permanent magnet system,” Materials Letters, **2**(5, Part 1), pp. 411-415.

[12] Guo H., Dong Z., Zhao D., Chen K., and Zhang X., 2003, “Development of permanent magnet systems for magnetic resonance imaging,” IEEE International Conference on Magnetics (INTERMAG 2003), p. GQ-13.

[13] Jameson E. C., 2001, Electrical Discharge Machining, Society of Manufacturing Engineers, Dearborn Michigan.

[14] Knight W. A., and Boothroyd G., 2005, Fundamentals of Metal Machining and Machine Tools, Third Edition (Mechanical Engineering, CRC Press.

[15] McGeough J. A., 1988, Advanced Methods of Machining, Springer.

[16] Zhang L., Abbott J. J., Dong L., Kratochvil B. E., Bell D., and Nelson B. J., 2009, “Artificial bacterial flagella: Fabrication and magnetic control,” Appl. Phys. Lett., **94**(6), p. 064107.

[17] Ghosh A., and Fischer P., 2009, “Controlled Propulsion of Artificial Magnetic Nanostructured Propellers,” Nano Letters, **9**(6), pp. 2243-2245.

[18] Mahoney A. W., Sarrazin J. C., Bamberg E., and Abbott J. J., 2011, “Velocity Control with Gravity Compensation for Magnetic Helical Microswimmers,” Advanced Robotics, **25**(8), pp. 1007–1028.

[19] Ishiyama K., Arai K. I., Sendoh M., and Yamazaki A., 2002, “Spiral-type micro-machine for medical applications,” Journal of Micromechatronics, **2**(1), pp. 77-86.

[20] Sendoh M., Ishiyama K., Arai K. I., Jojo M., Sato F., and Matsuki H., 2002, “Fabrication of magnetic micromachine for local hyperthermia,” Magnetics, IEEE Transactions on, **38**(5), pp. 3359-3361.

[21] Orino C., Rakwal D., Jorgnesen J. D., and Bamberg E., 2006, “Development of a precision, low-cost, small footprint wire electron discharge machine (WEDM),” Proceedings of the 2006 ASPE Conference, pp. 239-242.

[22] Rakwal D., Heamawatanachai S., Tathireddy P., Solzbacher F., and Bamberg E., 2009, “Fabrication of compliant high aspect ratio silicon microelectrode arrays using micro-wire electrical discharge machining,” Microsyst Technol, **15**(5), pp. 789-797.

[23] Rakwal D., and Bamberg E., 2009, “Slicing, cleaning and kerf analysis of germanium wafers machined by wire electrical discharge machining,” Journal of Materials Processing Technology, **209**(8), pp. 3740-3751.

[24] Rakwal D., and Bamberg E., 2007, "Using Taguchi Methods to Optimize the Slicing Rate and Surface Roughness for Wire Electrical Discharge Machining of P-type Germanium," Proc. 15th International Symposium on Electromachining (ISEM XV), Pittsburg, PA, pp. 127-132.

[25] Ross P. J., 1988, Taguchi Techniques for Quality Engineering: Loss Function, Orthogonal Experiments, Parameter and Tolerance Design, Mcgraw-Hill.

[26] Roy R. K., 1990, A Primer on the Taguchi Method, Van Nostrand Reinhold.

[27] ATI Industrial Automation, 2011, "Nano 17 Model Description," http://www.ati-ia.com/products/ft/ft_models.aspx?id=Nano17.

[28] Hiraga K., Hirabayashi M., Sagawa M., and Matsuura Y., 1985, "A Study of Microstructures of Grain Boundaries in Sintered Fe77Nd15 B8 Permanent Magnet by High-Resolution Electron Microscopy," Jpn. J. Appl. Phys., **24**(Part 1, No. 6), pp. 699-703.

[29] Baronzio G. F., and Hager E. D., 2006, Hyperthermia in cancer treatment: a primer, Springer.